bioRxiv preprint doi: https://doi.org/10.1101/2021.07.02.450848; this version posted July 4, 2021. The copyright holder for this preprint (which was not certified by peer review) is the author/funder, who has granted bioRxiv a license to display the preprint in perpetuity. It is made available under aCC-BY-NC-ND 4.0 International license.

Single-domain antibodies for targeting, detection and *in vivo* imaging of human CD4$^+$ cells

Bjoern Traenkle[1], Philipp D. Kaiser[1], Stefania Pezzana[2], Jennifer Richardson[3], Marius Gramlich[1], Teresa R. Wagner[1,4], Melissa Weldle[4], Stefanie Holz[4], Yana Parfyonova[4], Stefan Nueske[5], Armin M. Scholz[5], Anne Zeck[1], Meike Jakobi[1], Nicole Schneiderhan-Marra[1], Martin Schaller[6], Andreas Maurer[2,7], Cécile Gouttefangeas[3,7,8], Manfred Kneilling[2,6,7], Bernd J. Pichler[2,7,8], Dominik Sonanini[2,9], and Ulrich Rothbauer[1,4,7#]

Affiliations/Addresses

[1] NMI, Natural and Medical Sciences Institute at the University of Tuebingen, Reutlingen, Germany

[2] Werner Siemens Imaging Center, Department of Preclinical Imaging and Radiopharmacy, University of Tuebingen, Tuebingen, Germany

[3] Department of Immunology, Institute of Cell Biology, University of Tuebingen, Tuebingen, Germany

[4] Pharmaceutical Biotechnology, Eberhard Karls University Tuebingen, Germany

[5] Livestock Center of the Faculty of Veterinary Medicine, Ludwig Maximilians University Munich, Oberschleissheim, Germany

[6] Department of Dermatology, University of Tuebingen, Tuebingen, Germany

[7] Cluster of Excellence iFIT (EXC2180) "Image-Guided and Functionally Instructed Tumor Therapies", University of Tuebingen, Germany

[8] German Cancer Consortium (DKTK) and German Cancer Research Center (DKFZ) partner site Tuebingen, Tuebingen, Germany

[9] Department of Medical Oncology and Pneumology, University of Tuebingen, Tuebingen, Germany

[#] corresponding author

Prof. Dr. Ulrich Rothbauer, Natural and Medical Sciences Institute at the University of Tuebingen

bioRxiv preprint doi: https://doi.org/10.1101/2021.07.02.450848; this version posted July 4, 2021. The copyright holder for this preprint (which was not certified by peer review) is the author/funder, who has granted bioRxiv a license to display the preprint in perpetuity. It is made available under aCC-BY-NC-ND 4.0 International license.

Markwiesenstr. 55, 72770 Reutlingen, Germany.

E-mail: ulrich.rothbauer@uni-tuebingen.de

Phone: +49 7121 51530-415

Fax: +49 7121 51530-816

Orcid ID: 0000-0001-5923-8986

bioRxiv preprint doi: https://doi.org/10.1101/2021.07.02.450848; this version posted July 4, 2021. The copyright holder for this preprint (which was not certified by peer review) is the author/funder, who has granted bioRxiv a license to display the preprint in perpetuity. It is made available under aCC-BY-NC-ND 4.0 International license.

Abstract

The advancement of new immunotherapies for the treatment of cancers, infections, immune-mediated inflammatory diseases, and autoimmune diseases necessitates the co-development of appropriate probes to detect and monitor the distribution and infiltration of distinct immune cell populations. Considering the key role of $CD4^+$ T cells in regulating immunological processes, we have developed a set of novel single-domain antibodies (nanobodies, Nbs) that specifically recognize the human CD4 co-receptor in its native state on various $CD4^+$ cells. Following detailed characterization of binding properties, epitope mapping, and site-directed functionalization, we selected biologically inert Nbs that do not affect T cell proliferation or cytokine expression *in vitro*. We used fluorescently labeled Nbs to track the presence and location of $CD4^+$ cells in a xenograft model, demonstrating a high signal-to-background ratio by *in vivo* optical imaging. In summary, this study reports for the first time the generation and application of human CD4-specific Nbs for the detection and *in vivo* imaging of $CD4^+$ cells in a preclinical animal model. We anticipate that the Nbs presented in this study will be versatile probes, e.g. in immunoPET imaging for patient stratification and for monitoring individual immune responses during personalized immunotherapy.

bioRxiv preprint doi: https://doi.org/10.1101/2021.07.02.450848; this version posted July 4, 2021. The copyright holder for this preprint (which was not certified by peer review) is the author/funder, who has granted bioRxiv a license to display the preprint in perpetuity. It is made available under aCC-BY-NC-ND 4.0 International license.

Introduction

In precision medicine, diagnostic classification of the disease-associated immune status should guide the selection of appropriate therapies (1-3). A comprehensive analysis of a patient's specific immune cell composition, activation state, and infiltration of affected tissue has been shown to be highly informative for patient stratification. When administering immunotherapeutics, this enables the prediction of responders and non-responders, the monitoring of therapeutic efficacy, and the detection of serious adverse events even before symptoms occur (4-8). $CD4^+$ T cells are a key determinant of the immune status due to their essential role in orchestrating immune responses in T cell-mediated delayed hypersensitivity reactions in autoimmune diseases, inflammation, cancer, and chronic viral infections (9-16). Accordingly, detailed monitoring of the dynamic distribution of $CD4^+$ T cells is highly relevant for companion diagnostics. Currently, the presence, activation and differentiation state of $CD4^+$ T cells can be assessed and monitored in the peripheral blood of patients revealing only the systemic immune cell status. More comprehensive diagnostic measures from biopsies of tumors or of immune-mediated inflammatory diseases (IMIDs) are enabled by a range of methods including intra-cytoplasmic flow cytometry analysis (IC-FACS), cytometry by time of flight (CyTOF), immunohistochemistry and *ex vivo* cytokine assays or RT-PCR analysis (17-21). However, because of the heterogeneity of cancers and the $CD4^+$ T cell infiltrate in IMIDs, biopsies provide only spatially and temporally restricted information about the $CD4^+$ T cell infiltrate, which does often not reflect the holistic immune profile. Considering the emerging role of infiltrating lymphocytes and the impact of $CD4^+$ T cells on the outcome of immunotherapies novel approaches are needed to assess $CD4^+$ T cells throughout the entire tumor, all metastases, or the affected tissue of IMIDs (22, 23). In this context, non-invasive imaging approaches offer a significant benefit compared to the current diagnostic standard. To date, radiolabeled antibodies have been applied to image $CD4^+$ T cells in preclinical models (13, 24-26). Due to the recycling effect mediated by the neonatal Fc receptor, full-length antibodies have a long serum half-life (~ 1–3 weeks), which requires long clearance times (several days) before high-contrast images can be acquired (27). Additionally, effector function

bioRxiv preprint doi: https://doi.org/10.1101/2021.07.02.450848; this version posted July 4, 2021. The copyright holder for this preprint (which was not certified by peer review) is the author/funder, who has granted bioRxiv a license to display the preprint in perpetuity. It is made available under aCC-BY-NC-ND 4.0 International license.

via the Fc region was shown to induce depletion or functional changes in $CD4^+$ cells including the induction of proliferation or cytokine release (28-30). Notably, also higher dosages of recombinant antibody fragments like the Fab fragment or a Cys-diabody derived from the monoclonal anti-CD4 antibody GK1.5 were recently shown to cause a decrease in CD4 expression *in vivo* and inhibit proliferation and IFN-γ production *in vitro* (29-31). These studies highlight the importance of carefully investigating $CD4^+$ T cell-specific immunoprobes for their epitopes, binding properties, and functional effects.

During the last decade antibody fragments derived from heavy-chain-only antibodies of camelids (32), referred to as VHHs or nanobodies (Nbs) (32), emerge as novel probes for molecular imaging (reviewed in (33)). Nbs are characterized by a small size, antibody-like affinities and specificities, low off-target accumulation, high stability and good solubility (reviewed in (34, 35)). Their unique properties and ease of genetic and/or chemical functionalization offer significant advantages over conventional antibodies and recombinant fragments thereof. Additionally, Nbs were described as weakly immunogenic in humans due to their high homology to the human type 3 VH domain (VH3) (36). In combination with highly sensitive and/or quantitative whole-body molecular imaging techniques such as optical imaging or radionuclide-based techniques (e.g. positron emission tomography (PET)), Nbs have been shown to bind their targets within several minutes of systemic application (37). Due to their great potential as highly specific imaging probes, numerous Nbs targeting immune- or tumor-specific cellular targets are currently in preclinical development and even in clinical trials (33, 38, 39).

Here, we generated a set of human CD4-specific Nbs, examined their binding properties on recombinant and cellular CD4, and determined their epitopes with sub-domain resolution. A series of immunological analyses were performed to evaluate their impact on T cell proliferation and activation, as well as cytokine production in isolated human peripheral blood mononuclear cells (PBMCs) and whole blood. For non-invasive *in vivo* optical imaging, we converted the most promising candidates into CD4 immunoprobes by site-directed fluorescent labeling and investigated their ability to visualize human CD4-positive tissue in a murine xenograft model.

bioRxiv preprint doi: https://doi.org/10.1101/2021.07.02.450848; this version posted July 4, 2021. The copyright holder for this preprint (which was not certified by peer review) is the author/funder, who has granted bioRxiv a license to display the preprint in perpetuity. It is made available under aCC-BY-NC-ND 4.0 International license.

Results

Generation of high-affinity CD4 nanobodies

To generate Nbs directed against human CD4 (hCD4), we immunized an alpaca (*Vicugna pacos*) with the recombinant extracellular portion of hCD4 following an 87-day immunization protocol. Subsequently, we generated a Nb phagemid library comprising ~4 × 10^7 clones that represent the full repertoire of variable heavy chains of heavy-chain antibodies (VHHs or Nbs) of the animal. We performed phage display using either passively adsorbed purified hCD4 or CHO and HEK293 cells stably expressing full-length human CD4 (CHO-hCD4, HEK293-hCD4 cell lines). Following two cycles of phage display for each condition, we analyzed a total of 612 individual clones by whole-cell phage ELISA and identified 78 positive binders. Sequence analysis revealed 13 unique Nbs representing five different B cell lineages according to their complementarity determining regions (CDR) 3 (**Figure 1 A**). One representative Nb of each lineage, termed CD4-Nb1 – CD4-Nb5, was expressed in bacteria (*E.coli)* and isolated with high purity using immobilized metal ion affinity chromatography (IMAC) followed by size exclusion chromatography (SEC) (**Figure 1 B**). To test whether selected Nbs are capable of binding to full-length hCD4 localized at the plasma membrane of mammalian cells, we performed live-cell staining of CHO-hCD4 cells (**Figure 1 C, Supplementary Fig. 1**). Executed at 4°C, images showed a prominent staining of the plasma membrane, whereas at 37°C the fluorescent signal was mainly localized throughout the cell body, presumably a consequence of endocytotic uptake of receptor-bound Nbs. CHO wt cells were not stained by any of the five CD4-Nbs at both temperatures (data not shown). CD4-Nb1 and CD4-Nb3, both identified by whole-cell panning, displayed strong staining of CHO-hCD4 cells. Of the Nbs derived from panning with recombinant hCD4, CD4-Nb2 also showed strong cellular staining, whereas staining with CD4-Nb4 revealed weak signals. CD4-Nb5 showed no staining under these conditions and was consequently excluded from further analyses (**Figure 1 C**). To quantitatively assess binding affinities, we performed biolayer interferometry (BLI) measuring serial dilutions of Nbs on the biotinylated extracellular domain of hCD4 immobilized at the sensor tip. For CD4-Nb1 and CD4-Nb2, determined K_D values ~5 and ~7 nM, respectively,

bioRxiv preprint doi: https://doi.org/10.1101/2021.07.02.450848; this version posted July 4, 2021. The copyright holder for this preprint (which was not certified by peer review) is the author/funder, who has granted bioRxiv a license to display the preprint in perpetuity. It is made available under aCC-BY-NC-ND 4.0 International license.

while CD4-Nb3 and CD4-Nb4 displayed lower affinities of 75 nM and 135 nM, respectively (**Figure 1 D, Table 1, Supplementary Fig. 2 A**). In addition, we determined corresponding EC_{50} values with full-length plasma membrane-located hCD4 on HEK293-hCD4 cells by flow cytometry. In accordance with cellular staining and biochemically determined affinities these values revealed a strong functional binding for CD4-Nb1 and CD4-Nb2 with EC_{50} values in the subnanomolar range (~0.7 nM), whereas CD4-Nb3 and CD4-Nb4 displayed substantially lower cellular affinities (**Figure 1 E, Table 1, Supplementary Fig. 2 B**). In summary, we generated four CD4-Nbs that bind isolated as well as cell-resident hCD4. While CD4-Nb3 and CD4-Nb4 appeared less affine, CD4-Nb1 and CD4-Nb2 displayed high affinities in the low nanomolar range.

Domain mapping

Next, we applied chemo-enzymatic coupling using sortase A for site-directed functionalization of CD4-Nbs (40, 41). We thereby linked peptides conjugated to a single fluorophore to the C-terminus of CD4-Nbs yielding a defined labeling ratio of 1:1 (42). Live-cell immunofluorescence imaging showed that all sortase-coupled CD4-Nbs retained their capability of binding to cell-resident hCD4 of CHO-hCD4 cells (**Supplementary Fig. 3 A**). To localize the binding sites of the selected CD4-Nbs, we generated domain-deletion mutants of hCD4. Expression and correct surface localization of these mutants in CHO cells was confirmed by staining with antibody RPA-T4 binding to domain 1 of CD4. For mutants lacking domain 1, we introduced an N-terminal BC2 tag (43) to allow for live-cell surface detection with a fluorescently labeled bivBC2-Nb (42) (**Supplementary Fig. 3 B**). Transiently expressed domain-deletion mutants were then tested for binding of CF568-labeled CD4-Nbs by live-cell immunofluorescence imaging, including a non-specific fluorescently labeled GFP-binding Nb (GFP-Nb) as negative control. Based on these results, we allocated binding of CD4-Nb1 and CD4-Nb3 to domain 1, whereas CD4-Nb2 and CD4-Nb4 bind to domain 3 and/or 4 of hCD4 (**Figure 2 A, Supplementary Fig. 3 C**).

bioRxiv preprint doi: https://doi.org/10.1101/2021.07.02.450848; this version posted July 4, 2021. The copyright holder for this preprint (which was not certified by peer review) is the author/funder, who has granted bioRxiv a license to display the preprint in perpetuity. It is made available under aCC-BY-NC-ND 4.0 International license.

To further examine combinatorial binding of the different CD4-Nbs, we performed an epitope binning analysis by BLI. Recombinant full-length hCD4 was immobilized at the sensor tip and combinations of CD4-Nbs were allowed to bind consecutively (**Supplementary Fig. 4**). Unsurprisingly, CD4-Nbs binding to different domains, displayed combinatorial binding. Interestingly, a simultaneous binding was also detected for the combination of CD4-Nb1 and CD4-Nb3, suggesting that both CD4-Nbs bind to different epitopes within domain 1. In contrast, we did not observe simultaneous binding for CD4-Nb2 and CD4-Nb4, which might be due to close-by or overlapping epitopes at domain 3/4 for the latter Nb pair.

For a more precise epitope analysis, we conducted a hydrogen-deuterium-exchange (HDX) mass spectrometry analysis of hCD4 bound to CD4-Nb1, CD4-Nb2 or CD4-Nb3 (**Figure 2 B-E**). Due to its low affinity, CD4-Nb4 was not considered for HDX-MS analysis (data not shown). In accordance with our previous findings, binding of CD4-Nb1 and CD4-Nb3 protected sequences of domain 1 from HDX, whereas CD4-Nb2 protected sequences of domain 3 and 4 of hCD4 (**Figure 2 B**). The results obtained for binding of CD4-Nb1 (**Figure 2 C**) are similar to those obtained for CD4-Nb3 (**Figure 2 D**) in that binding of either Nb reduced hydrogen exchange at amino acid residues (aa) from aa T17 to N73, albeit with a different extent of protection at individual sequence segments. For CD4-Nb1 the greatest protection from HDX was observed for the sequence ranging from aa K35 – L44 corresponding to β strand C´ and C´´ of the immunoglobulin fold of domain 1 and residues aa K46 – K75, comprising β strands D and E. In contrast, binding of CD4-Nb3 confers only a minor reduction in HDX within the latter sequence, but additionally protects sequence aa C84 – E91, which correspond to β strands G and F and their intermediate loop. For CD4-Nb2 we found protection of sequences aa W214 – F229 (β strands C and C´) and aa K239 – L259 (β strands C´´-E), and to a minor extend sequence aa R293 - L296 as part of β strands A of domain 4 (**Figure 2 E**). In summary, our HDX-MS analysis revealed that all three tested Nbs bind three dimensional epitopes within different parts of hCD4. It further provides an explanation how CD4-Nb1 and CD4-Nb3 can bind simultaneously to domain 1 of hCD4, and confirms that the epitope of CD4-Nb2 is mainly located at domain 3.

bioRxiv preprint doi: https://doi.org/10.1101/2021.07.02.450848; this version posted July 4, 2021. The copyright holder for this preprint (which was not certified by peer review) is the author/funder, who has granted bioRxiv a license to display the preprint in perpetuity. It is made available under aCC-BY-NC-ND 4.0 International license.

Binding of CD4-Nbs to human PBMCs

Having demonstrated that all selected Nbs bind to recombinant and exogenously overexpressed cellular hCD4, we next examined their capability and specificity of binding to physiologically relevant levels of $CD4^+$ T cells within PBMC samples. We co-stained human PBMCs from three donors with CD4-Nbs1-4 coupled to CF568 (100 nM for high-affine CD4-Nb1 and CD4-Nb2; 1000 nM for low-affine CD4-Nb3 and CD4-Nb4) in combination with an anti-CD3 antibody and analyzed the percentage of double-positive cells ($CD3^+CD4^+$) by flow cytometry (**Figure 3 A, Supplementary Fig. 5**). Compared to staining with an anti-CD4 antibody used as positive control, all CD4-Nbs stained a similar percentage of $CD4^+$ T cells for all tested donors, while the non-specific GFP-Nb yielded a negligible percentage of double-positive cells even at the highest concentration (1000 nM) (**Figure 3 B, Table 2**).

Impact of CD4-Nbs on activation, proliferation and cytokine release of $CD4^+$ T and immune cells

Towards the envisioned application as clinical imaging tracer, we next assessed basic issues associated with CD4-Nbs, regarding their influence on the activation, proliferation and cytokine release of $CD4^+$ T cells. First, to exclude adverse effects of bacterial endotoxins present in the CD4-Nbs1-4 preparations, we attempted to remove endotoxins by depletion chromatography to yield FDA-acceptable endotoxin levels of <0.25 EU per mg. While this was achieved for CD4-Nb1, CD4-Nb4 and the non-specific GFP-Nb, we failed to lower protein-associated endotoxins to acceptable levels for CD4-Nb2 and CD4-Nb3 even after repeated depletion chromatography. Consequently, we continued these experimental studies only with CD4-Nb1, CD4-Nb4 and GFP-Nb as control. In brief, carboxyfluorescein succinimidyl ester (CFSE)-labeled human PBMCs from three pre-selected healthy donors were pre-treated with CD4-Nbs or a control Nb at concentrations between 0.05 µM – 5 µM for 1 h at 37°C, mimicking the expected approximate concentration and serum retention time during clinical *in vivo* imaging application. Cells were then washed to remove Nbs and stimulated with an antigenic (cognate MHCII peptides) or a non-antigenic stimulus (phytohaemagglutinin, PHA-L) and analyzed after

bioRxiv preprint doi: https://doi.org/10.1101/2021.07.02.450848; this version posted July 4, 2021. The copyright holder for this preprint (which was not certified by peer review) is the author/funder, who has granted bioRxiv a license to display the preprint in perpetuity. It is made available under aCC-BY-NC-ND 4.0 International license.

4, 6 and 8 days by flow cytometry with the gating strategy shown in **Supplementary Fig. 6 A**. According to the highly similar CFSE intensity profiles observed, the total number of cell divisions was not affected by the different Nb treatments (exemplarily shown for one of three donors on day 6, **Supplementary Fig. 6 A**). For samples of the same donor and time point, no substantial differences in the percentage of proliferated cells were observed between mock incubation and individual Nb treatments.

For both stimuli, the average percentage of proliferated cells increased over time in all donors tested, with no clear differences between conditions (**Figure 4 A**). As quantitative measure of T cell activation, we also determined the cell surface induction of a very early activation marker (CD69) and of the IL-2 receptor α chain (CD25) on $CD4^+$ T cells (**Figure 4 B**). Among samples of the same donor and stimulation, we found highly similar activation profiles for all Nb treatments. While the percentage of $CD4^+CD25^+$ cells steadily increased over time for MHCII peptide stimulation, for PHA-stimulated condition the percentage of positive cells was similarly high at all times of analysis. Importantly, regardless of the differences between donors, the individual Nb treatments from the same donor did not result in significant differences in the percentage of $CD4^+CD25^+$ or $CD4^+CD69^+$ cells for either stimulation at any point in the analysis.

Next, we analyzed cytokine expression of $CD4^+$ T cells by intracellular cytokine staining after restimulation with cognate MHCII peptides. The corresponding gating strategy is shown in **Supplementary Fig. 6 B**. Samples of the same donor treated with different Nbs had highly similar percentages of cytokine (TNF, IFN-γ or IL-2) or activation marker (CD154)-positive cells without stimulation and upon stimulation with MHCII peptides (**Figure 4 C**). Overall, exposure to CD4-Nbs did not affect proliferation, activation or cytokine production of $CD4^+$ T cells. In addition, we analyzed potential effects of CD4-Nbs on the release of cytokines from full-blood samples of three further donors. Upon stimulation with lipopolysaccharide (LPS) or PHA-L, we determined the serum concentrations with a panel of pro- and anti-inflammatory cytokines (**Supplementary Table S2**). Although there was significant inter-donor variation for some

bioRxiv preprint doi: https://doi.org/10.1101/2021.07.02.450848; this version posted July 4, 2021. The copyright holder for this preprint (which was not certified by peer review) is the author/funder, who has granted bioRxiv a license to display the preprint in perpetuity. It is made available under aCC-BY-NC-ND 4.0 International license.

cytokines, Nb treatment did not result in significant differences in either stimulated or unstimulated samples (**Supplementary Fig. 7**).

In vivo optical imaging of CD4-Nbs

For optical *in vivo* imaging, we labeled CD4-Nbs with the fluorophore Cy5.5 (CD4-Nb-Cy5.5) by sortase-mediated attachment of an azide group followed by click-chemistry addition of DBCO-Cy5.5. First, we tested potential cross-reactivity of the four Cy5.5-labeled CD4-Nbs to murine $CD4^+$ lymphocytes. Notably, flow cytometric analysis showed that none of the selected CD4-Nbs was able to bind murine $CD4^+$ cells, suggesting exclusive binding to human CD4. Moreover, low-affine binding CD4-Nb4 bound neither mouse nor human $CD4^+$ cells at the concentration used here (0.75 µg/ml, ~49 nM) (**Supplementary Fig. 8**). Consequently, we focused on CD4-Nb1 as the most promising candidate and CD4-Nb4 as a candidate with a high off-target rate, both of which we further analyzed for their *in vivo* target specificity and dynamic distribution using a murine xenograft model.

To establish human $CD4^+$ expressing tumors, NSG mice were inoculated subcutaneously with $CD4^+$ T cell leukemia HPB-ALL cells (44). After 2 – 3 weeks, mice bearing HPB-ALL xenografts were injected with 5 µg of CD4-Nb1-Cy5.5, CD4-Nb4-Cy5.5, or a control Nb (GFP-Nb-Cy5.5) and optically imaged in intervals over the course of 24 h (**Figure 5 A**, **Supplementary Fig. 9 A**). The Cy5.5 signal intensity (SI) of the control Nb peaked within 10 – 20 minutes and rapidly declined thereafter to approximately the half and a quarter of maximum level at 2 h and 24 h, respectively (**Figure 5 B**, **Supplementary Fig. 9 B**). While the SI of the low-affinity CD4-Nb4-Cy5.5 did not exceed the SI of the control Nb at any time (**Supplementary Fig. 9 B**), CD4-Nb1-Cy5.5 reached its maximum SI within the HPB-ALL xenograft of ~1.8-fold above the control Nb, at 30 min and slowly declined to ~90% and ~80% of maximum after 2 and 4 hours, respectively (**Figure 5 B**). Based on the differences in the SI between CD4-Nb1-Cy5.5 and GFP-Nb-Cy5.5, we observed the optimal target accumulation and specificity between 60 and 120 min post injection (**Figure 5 B**). After 24 h, mice were euthanized, and the presence of fluorophore-labeled CD4 Nbs within the explanted tumors was analyzed by optical imaging

bioRxiv preprint doi: https://doi.org/10.1101/2021.07.02.450848; this version posted July 4, 2021. The copyright holder for this preprint (which was not certified by peer review) is the author/funder, who has granted bioRxiv a license to display the preprint in perpetuity. It is made available under aCC-BY-NC-ND 4.0 International license.

(OI) (**Figure 5 C, Supplementary Fig. 9 C**). Compared to control, tumors from mice injected with CD4-Nb1-Cy5.5 had ~4-fold higher Cy5.5 SI, indicating a good signal-to-background ratio for this Nb-derived fluorescently labeled immunoprobe. To confirm CD4-specific targeting of CD4-Nb1 within the xenograft, we performed *ex vivo* immunofluorescence of HPB-ALL tumors at 2 h and 24 h post injection (**Supplementary Fig. 10**). At the early time point, when the *in vivo* OI signal peaked, CD4-Nb1 was widely distributed throughout the whole tumor whereas no Cy5.5 signal was detected in the GFP-Nb-injected mice (**Supplementary Fig. 10 A, B**). Semiquantitative analysis at the single-cell level revealed intense CD4-Nb1 binding at the surface of HBP-ALL cells that correlated with the CD4 antibody signal and internalization of CD4-Nb1 in some cells (**Supplementary Fig. 10 C**). Upon administration of unrelated GFP-Nb, no Nb binding was observed (**Supplementary Fig. 10 D**). 24 h post injection we observed regions of strongly internalized CD4-Nb1 (**Supplementary Fig. 10 E, G**), but also regions showing a low residual CD4-Nb1 uptake (**Supplementary Fig. 10 E, H**).

Although the HBP-ALL xenograft model used for *in vivo* imaging does not reflect the natural distribution of $CD4^+$ T cells in an organism, the provided data strongly indicates that high-affinity binding CD4-Nb1 is suitable for visualizing $CD4^+$ cells *in vivo* by non-invasive imaging.

bioRxiv preprint doi: https://doi.org/10.1101/2021.07.02.450848; this version posted July 4, 2021. The copyright holder for this preprint (which was not certified by peer review) is the author/funder, who has granted bioRxiv a license to display the preprint in perpetuity. It is made available under aCC-BY-NC-ND 4.0 International license.

Discussion

Prognosis and therapeutic susceptibility to immunotherapies are critically influenced by the presence and activity of various subsets of immunological cells, including members of the innate and adaptive immunity. The role of immune cells in influencing the outcome of e.g. cancer therapy, is generally recognized (45, 46). Among the latter, T cells acquire functional and effector phenotypes whose activities have direct pro- or anti-inflammatory consequences (47). In this context, $CD4^+$ T helper 1 (Th1) cells for example promote anti-tumoral responses by secretion of proinflammatory cytokines such as IL-2, TNF, and IFN-γ, which promotes cytotoxic $CD8^+$ T cell (CTL) priming and cytotoxicity (48). CD4, a co-receptor of the T cell receptor (TCR) complex, is predominantly expressed by T helper and regulatory T cells and plays an important role in the recognition of major histocompatibility complex class II (MHCII) molecules expressed on antigen-presenting cells (49). In addition, minor levels of CD4 are also expressed on monocytes, macrophages, NK cells and dendritic cells. Upon interaction of CD4 with MHCII, $CD4^+$ T cells become activated, recruiting other immune cells and assist the transformation of B cells to antibody-producing plasma cells and thereby guiding pro- and anti-inflammatory responses. With respect to cancer, the presence of infiltrating $CD4^+$ Th1 cells in tumors correlates with a favorable prognosis in terms of overall survival and disease-free survival in many malignancies (48). However, cancer cells can also recruit regulatory $CD4^+$ T cells (Tregs), which suppress many of the anti-tumor activities and have been reported to negatively regulate CTLs and activated $CD4^+$ T cells by exploiting the peripheral tolerance mechanism via checkpoint engagement (50-53).

Given this important role of $CD4^+$ T cells, their detailed monitoring is proving to be highly relevant for the concomitant diagnosis not only of cancer (reviewed in (12)), but also of other diseases, including viral infections (13-16) and autoimmune diseases (9-11). Several mouse studies and early clinical trials already indicated the value of non-invasive imaging of $CD4^+$ cells in rheumatoid arthritis (25), colitis (26), allogenic stem cell transplantation (54), organ transplant rejection (55), acquired immunodeficiency disease (13), and in the context of cancer immunotherapies (56), using radiolabeled full-length antibodies or fragments thereof.

bioRxiv preprint doi: https://doi.org/10.1101/2021.07.02.450848; this version posted July 4, 2021. The copyright holder for this preprint (which was not certified by peer review) is the author/funder, who has granted bioRxiv a license to display the preprint in perpetuity. It is made available under aCC-BY-NC-ND 4.0 International license.

However, biological activity, particularly CD4$^+$ T cell depletion, and long-term systemic retention of full-length antibodies limit their development into clinically applied immunoprobes (25, 29, 57, 58).

In this study, we developed novel Nbs as immunoprobes for the visualization and monitoring of human CD4$^+$ cells in various biomedical research applications, focusing on non-invasive *in vivo* imaging. To identify binders that recognize the cellular exposed CD4 receptor, we generated a Nb phage display library from an alpaca immunized with the extracellular portion of recombinant human CD4 and employed two screening strategies. First, we performed phage display against adsorbed recombinant CD4 and second, we used whole cells stably expressing human CD4. Interestingly, both strategies proved successful, as demonstrated by the selection of two Nbs that efficiently bind cell-resident CD4 from each panning strategy.

To determine key information regarding their stabilities, affinities, and recognized epitopes on human CD4, these Nbs were subjected to in-depth biochemical characterization. Using epitope binning, cellular imaging, and HDX-MS, we were able to elucidate in detail the detected domains, as well as the three-dimensional epitopes addressed by the individual Nbs, and thus identified two candidates, CD4-Nb1 and CD4-Nb3, that can simultaneously bind different segments within domain 1, while CD4-Nb2 has been shown to bind domain 3 of CD4. Notably, such detailed information is not available for most Nbs currently developed for *in vivo* imaging (59-65). However, for CD4-specific Nbs this knowledge is all the more important because epitope-specific targeting of CD4$^+$ T cell functions have far-reaching implications. This is true especially for cancer treatment, as CD4$^+$ cells have opposing effects on tumor growth and response to immunotherapies, crucially depending on the CD4 effector cell differentiation and tumor entity (66, 67). In this context it was shown that domain 1 of CD4 mediates transient interaction of the CD4 receptor and the MHCII complex (68-70), while T cell activation is abrogated when TCR and CD4 colocalization is blocked via domain 3 (71).

To further elucidate a possible impact on immunomodulation, we analyzed the effect of CD4-Nb1 and CD4-Nb4 targeting two different domains on CD4$^+$ T cell proliferation and cytokine expression. Notably, here we used Nb concentrations as they are proposed to be applied for

bioRxiv preprint doi: https://doi.org/10.1101/2021.07.02.450848; this version posted July 4, 2021. The copyright holder for this preprint (which was not certified by peer review) is the author/funder, who has granted bioRxiv a license to display the preprint in perpetuity. It is made available under aCC-BY-NC-ND 4.0 International license.

molecular imaging purposes in patients. In summary, none of the Nbs seems to affect the behavior of endogenous CD4$^+$ T cells *in vitro* or induce increased cytokine levels in whole blood samples. From these data it can be concluded that these Nbs are mostly biologically inert and thus might be beneficial compared to full-length antibodies (29) or other antibody fragments such as the anti-CD4 cys-diabody, which was recently reported to inhibit proliferation of CD4$^+$ cells and IFN-γ production *in vitro* (31).

Finally, we provide first data on the performance of our CD4-Nbs for *in vivo* imaging applications. Facing the challenge that the selected CD4 Nbs bind exclusively to human CD4 but not to the homolog in mice, we used a murine xenograft model in which we implemented a CD4$^+$ T leukemia tumor model based on human-derived HBP-ALL cells. For optical imaging, we performed a site-directed labeling approach employing C-terminal sortagging to conjugate an azide group, which can be universally used to attach a multitude of detectable moieties by straightforward DBCO-mediated click chemistry (59). By optical *in vivo* imaging, we monitored the specific enrichment of the high-affine CD4-Nb1 but not of the low-affine CD4-Nb4 on HBP-ALL-derived xenografts. A twofold signal-to-background ratio within 120 min after application and a rapid decrease in Nb-derived fluorescence intensities after 24 h suggest that the CD4-Nb1 is well suited to identify CD4$^+$ cells *in vivo*.

Undoubtedly, these first promising results still need to be confirmed in a more physiologically relevant *in vivo* model. Therefore, we are considering a humanized CD4 mouse model to further investigate CD4-Nb1-mediated visualization of CD4$^+$ T cells under physiologically relevant conditions. In parallel, we have begun to convert our CD4 Nbs into corresponding radiolabeled immunoPET imaging probes using the combination of sortagging and subsequent click-mediated, site-directed attachment of the detectable portion, as described in this study. We propose that PET imaging with radiolabeled CD4-Nbs will meet the clinical needs of tracking CD4$^+$ T cells non-invasively with high resolution and appropriate sensitivity.

As mentioned previously, epitope-specific targeting of CD4$^+$ T cell functions by Nbs might also be beneficial for novel therapeutic approaches (72). Consequently, beyond application as a diagnostic agent, CD4 Nbs offer various therapeutic opportunities. We now have started to

bioRxiv preprint doi: https://doi.org/10.1101/2021.07.02.450848; this version posted July 4, 2021. The copyright holder for this preprint (which was not certified by peer review) is the author/funder, who has granted bioRxiv a license to display the preprint in perpetuity. It is made available under aCC-BY-NC-ND 4.0 International license.

investigate the impact of targeted binding of mono- or biparatopic CD4 Nbs to modulate protein interactions and downstream signaling of CD4, thus exploiting the potential of Nbs as functional modulators.

In summary, this study demonstrates for the first time the generation and detailed characterization of Nbs specific for human CD4 and their comprehensive experimental evaluation *in vitro* and *in vivo*. In particular, CD4-Nb1 is a promising candidate for the non-invasive, whole-body study of $CD4^+$ T cells in mice, as well as in humans. In the next step, we will convert the CD4-Nb1 into an immunoPET tracer to quantify and monitor the infiltration of $CD4^+$ T cells in different tumor types using a humanized CD4 mouse model.

bioRxiv preprint doi: https://doi.org/10.1101/2021.07.02.450848; this version posted July 4, 2021. The copyright holder for this preprint (which was not certified by peer review) is the author/funder, who has granted bioRxiv a license to display the preprint in perpetuity. It is made available under aCC-BY-NC-ND 4.0 International license.

Data availability

The data that support the findings of this study are available from the corresponding author upon reasonable request.

Authorship Contributions

B.T., M.K., D.S., B.P. and U.R. designed the study; S.N., A.S. immunized the animal; P.D.K., S.H., Y.P. performed Nb selection; P.D.K, B.T., M.W., T.R.W., A.M. performed biochemical characterization and functionalization of Nbs; M.G., A.Z. performed MS analysis; A.Z. and M.G. performed HDX-MS experiments; J.R., C.G., M.J., N.S.M. analyzed the Nb effects on T cell proliferation and cytokine expression; S.P., and D.S. performed *in vivo* imaging; M.S. performed staining of xenograft cryosections; B.T., J.R., C.G., M.K., B.P., D.S. and U.R. drafted the manuscript; M.K., B.P. and U.R. supervised the study.

Competing financial interests

D.S., M.K., B.P., B.T., P.D. K., U.R. are named as inventors on a patent application claiming the use of the described nanobodies for diagnosis and therapeutics filed by the Natural and Medical Sciences Institute and the Werner Siemens Imaging Center. The other authors declare no competing interest.

Acknowledgements

This work received financial support from the State Ministry of Baden-Wuerttemberg for Economic Affairs, Labour and Tourism (Grant: Predictive diagnostics of immune-associated diseases for personalized medicine. FKZ: 35-4223.10/8). The authors thank Sandra Maier and Ulrich Kratzer (both Natural and Medical Sciences Institute at the University of Tuebingen) for technical support with MS analyses, and Birgit Fehrenbacher (Department of Dermatology, University of Tuebingen) for technical support with imaging of xenograft cryosections.

bioRxiv preprint doi: https://doi.org/10.1101/2021.07.02.450848; this version posted July 4, 2021. The copyright holder for this preprint (which was not certified by peer review) is the author/funder, who has granted bioRxiv a license to display the preprint in perpetuity. It is made available under aCC-BY-NC-ND 4.0 International license.

Materials and Methods

Nanobody library generation

Alpaca immunization and Nb library construction were carried out as described previously (73, 74). Animal immunization has been approved by the government of Upper Bavaria (Permit number: 55.2-1-54-2532.0-80-14). In brief, an alpaca (*Vicugna pacos*) was immunized with the purified extracellular domains of human CD4 (aa26-390) recombinantly produced in HEK293 cells (antibodies-online GmbH, Germany). After initial priming with 1 mg, the animal received six boost injections with 0.5 mg hCD4 each, every second week. 87 days after initial immunization, ~100 ml of blood were collected and lymphocytes were isolated by Ficoll gradient centrifugation using Lymphocyte Separation Medium (PAA Laboratories GmbH). Total RNA was extracted using TRIzol (Life Technologies) and mRNA was transcribed into cDNA using the First-Strand cDNA Synthesis Kit (GE Healthcare). The Nb repertoire was isolated in 3 subsequent PCR reactions using the following primer combinations (1) CALL001 and CALL002, (2) forward primer set FR1-1, FR1-2, FR1-3, FR1-4 and reverse primer CALL002, and (3) forward primer FR1-ext1 and FR1-ext2 and reverse primer set FR4-1, FR4-2, FR4-3, FR4-4, FR4-5 and FR4-6 introducing SfiI and NotI restriction sites. The Nb library was subcloned into the SfiI/ NotI sites of the pHEN4 phagemid vector (75).

Nb screening

For the selection of CD4-specific Nbs two consecutive phage enrichment rounds were performed, both with immobilized recombinant antigen and CHO-hCD4 cells. *E.coli* TG1 cells comprising the hCD4-Nb-library in pHEN4 were infected with the M13K07 helper phage to generate Nb-presenting phages. For each round 1×10^{11} phages of the hCD4-Nb-library were applied on immunotubes coated with hCD4 (10 µg/ml). In each selection round extensive blocking of antigen and phages was performed with 5% milk or BSA in PBS-T and with increasing panning rounds PBS-T washing stringency was increased. Bound phages were eluted in 100 mM tri-ethylamine, TEA (pH10.0), followed by immediate neutralization with 1 M Tris/HCl pH7.4. For cell-based panning, 2×10^{6} CHO-hCD4 or HEK293-hCD4 were non-

bioRxiv preprint doi: https://doi.org/10.1101/2021.07.02.450848; this version posted July 4, 2021. The copyright holder for this preprint (which was not certified by peer review) is the author/funder, who has granted bioRxiv a license to display the preprint in perpetuity. It is made available under aCC-BY-NC-ND 4.0 International license.

enzymatically detached using dissociation buffer (Gibco) and suspended in 5% fetal bovine serum (FBS) in PBS. Antigen expressing cells were incubated with 1×10^{11} phages under constant mixing at 4°C for 3 h. Cells were washed 3 × with 5% FBS in PBS. Cell lines were alternated between panning rounds. Phages were eluted with 75 mM citric acid buffer at pH2.3 for 5 min. To deplete non-CD4-specific phages, eluted phages were incubated 3 × with 1×10^{7} wt cells. Exponentially growing E.coli TG1 cells were infected with eluted phages from both panning strategies and spread on selection plates for following panning rounds. Antigen-specific enrichment for each round was monitored by counting colony forming unit (CFUs).

Whole-cell phage ELISA

Polystyrene Costar 96-well cell culture plates (Corning) were coated with poly-L-lysine (Sigma Aldrich) and washed once with H_2O. CHO-wt and CHO-hCD4 were plated at 2×10^{4} cells per well in 100 µl and grown to confluency overnight. Next day, 70 µl of phage supernatant was added to culture medium of each cell type and incubated at 4°C for 3 h. Cells were washed 5 × with 5% FBS in PBS. M13-HRP-labeled antibody (Progen) was added at a conc. 0.5 ng/ml for 1 h, washed 3 × with 5% FBS in PBS. Onestep ultra TMB 32048 ELISA substrate (Thermo Fisher Scientific) was added and incubated until color change was visible and the reaction was stopped by addition of 100 µl of 1M H_2SO_4. Detection occurred at 450 nm at a Pherastar plate reader and phage ELISA-positive clones were defined by a 2-fold signal above wt control cells.

Expression constructs

The cDNA of human CD4 (UniProtKB - P01730) was amplified from hCD4-mOrange plasmid DNA (hCD4-mOrange was a gift from Sergi Padilla Parra; addgene plasmid #110192; http://n2t.net/addgene:110192; RRID:Addgene_110192) by PCR using forward primer hCD4 fwd and reverse primer hCD4 rev and introduced into BamHI and XhoI sites of a pcDNA3.1 vector variant (pcDNA3.1(+)IRES GFP, a gift from Kathleen_L Collins; addgene plasmid #51406; http://n2t.net/addgene:51406; RRID:Addgene_51406). We replaced the neomycin resistance gene (NeoR) with the cDNA for Blasticidin S deaminase (bsd), amplified with

bioRxiv preprint doi: https://doi.org/10.1101/2021.07.02.450848; this version posted July 4, 2021. The copyright holder for this preprint (which was not certified by peer review) is the author/funder, who has granted bioRxiv a license to display the preprint in perpetuity. It is made available under aCC-BY-NC-ND 4.0 International license.

forward primer bsd fwd and reverse primer bsd rev, by integration into the XmaI and BssHII sites of the vector. CD4 domain deletion mutants were generated using the Q5 Site-Directed Mutagenesis Kit (NEB) according to the manufacturer´s protocol. For mutants lacking domain 1 of hCD4 we introduced an N-terminal BC2-tag (43). For the generation of plasmid pcDNA3.1_CD4_ΔD1_IRES-eGFP we used forward primer ΔD1 fwd and reverse primer ΔD1 rev; for pcDNA3.1_CD4_ΔD1ΔD2_IRES-eGFP forward primer ΔD1ΔD2 fwd and reverse primer ΔD1ΔD2 rev; for pcDNA3.1_CD4_ΔD3ΔD4_IRES-EGFP forward primer ΔD3ΔD4 fwd and reverse primer ΔD3ΔD4 rev. For bacterial expression of Nbs, sequences were cloned into the pHEN6 vector (76), thereby adding a C-terminal sortase tag LPETG followed by 6xHis-tag for IMAC purification as described previously (42). For protein production of the extracellular domains 1-4 of hCD4 in Expi293 cells, corresponding cDNA was amplified from plasmid DNA containing full-length human CD4 cDNA (addgene plasmid #110192) using forward primer CD4-D1-4 f and reverse primer CD4-D1-4 r. A 6xHis tag was introduced by the reverse primer. Esp3I and EcoRI restriction sites were used to introduce the cDNA into a pcDNA3.4 expression vector with the signal peptide MGWTLVFLFLLSVTAGVHS from the antibody JF5 (77).

Cell culture, transfection, stable cell line generation

HEK293T and CHO-K1 cells were obtained from ATCC (CCL-61, LGC Standards GmbH, Germany). As this study does not include cell line-specific analysis, cells were used without additional authentication. Cells were cultivated according to standard protocols. Briefly, growth media containing DMEM (HEK293) or DMEM/F12 (CHO) (both high glucose, pyruvate, Thermo Fisher Scientific (TFS)) supplemented with 10% (v/v) FBS, L-glutamine and penicillin/streptomycin (P/S; all from TFS) were used for cultivation. Cells were passaged using 0.05% trypsin-EDTA (TFS) and were cultivated at 37°C and 5% CO_2 atmosphere in a humidified chamber. Plasmid DNA was transfected using Lipofectamine 2000 (TFS) according to the manufacturer's protocol. For the generation of the stable HEK293-hCD4 and CHO-hCD4 cell line, 24 h post transfection, cells were subjected to a two-week selection period using 5 µg/ml Blasticidin S (Sigma Aldrich) followed by single cell separation. Individual clones were

bioRxiv preprint doi: https://doi.org/10.1101/2021.07.02.450848; this version posted July 4, 2021. The copyright holder for this preprint (which was not certified by peer review) is the author/funder, who has granted bioRxiv a license to display the preprint in perpetuity. It is made available under aCC-BY-NC-ND 4.0 International license.

analyzed by live-cell fluorescence microscopy regarding their level and uniformity of GFP and CD4 expression.

Protein expression and purification

CD4-specific Nbs were expressed and purified as previously published (74, 78). Extracellular fragment of human CD4 comprising domains 1-4 of human CD4 and a C-terminal His6-tag was expressed in Expi293 cells according to the manufacturer´s protocol (Thermo Fisher Scientific). Cell supernatant was harvested by centrifugation 4 days after transfection, sterile filtered and purified according to previously described protocols (79). For quality control, all purified proteins were analyzed via SDS-PAGE according to standard procedures. Therefore, protein samples were denaturized (5 min, 95°C) in 2x SDS-sample buffer containing 60 mM Tris/HCl, pH6.8; 2% (w/v) SDS; 5% (v/v) 2-mercaptoethanol, 10% (v/v) glycerol, 0.02% bromphenole blue. All proteins were visualized by InstantBlue Coomassie (Expedeon) staining. For immunoblotting proteins were transferred to nitrocellulose membrane (Bio-Rad Laboratories) and detection was performed using anti-His primary antibody (Penta-His Antibody, #34660, Qiagen) followed by donkey-anti-mouse secondary antibody labeled with AlexaFluor647 (Invitrogen) using a Typhoon Trio scanner (GE-Healthcare, excitation 633 nm, emission filter settings 670 nm BP 30).

Live-cell immunofluorescence

CHO-hCD4, and CHO wt cells transiently expressing CD4 domain-deletion mutants were plated at ~10,000 cells per well of a µClear 96-well plate (Greiner Bio One, cat. #655090) and cultivated at standard conditions. Next day, medium was replaced by live-cell visualization medium DMEMgfp-2 (Evrogen, cat. #MC102) supplemented with 10% FBS, 2 mM L-glutamine, 2 µg/ml Hoechst33258 (Sigma Aldrich) for nuclear staining, and fluorescently labeled or unlabeled CD4-Nbs at concentrations between 1 nM and 100 nM. Unlabeled CD4-Nbs were visualized by addition of 2.5 µg/ml anti-VHH secondary Cy5 AffiniPure Goat Anti-

bioRxiv preprint doi: https://doi.org/10.1101/2021.07.02.450848; this version posted July 4, 2021. The copyright holder for this preprint (which was not certified by peer review) is the author/funder, who has granted bioRxiv a license to display the preprint in perpetuity. It is made available under aCC-BY-NC-ND 4.0 International license.

Alpaca IgG (Jackson Immuno Research). Images were acquired with a MetaXpress Micro XL system (Molecular Devices) at 20× or 40× magnification.

Biolayer interferometry (BLI)

To determine the binding affinity of purified Nbs to recombinant hCD4, biolayer interferometry (BLItz, ForteBio) was performed. First, CD4 was biotinylated by 3-fold molar excess of biotin-N-hydroxysuccinimide ester. CD4 was then immobilized at single-use streptavidin biosensors (SA) according to manufacturer's protocols. For each Nb we executed four association/dissociation runs with concentrations appropriate for the affinities of the respective nanobodies (overall between 15.6 nM and 1 µM). As a reference run, PBS was used instead of Nb in the association step. As negative control the GFP-Nb (500 nM) was applied in the binding studies. Recorded sensograms were analyzed using the BLItzPro software and dissociation constants (K_D) were calculated based on global fits. For the epitope competition analysis, two consecutive application steps were performed, with a short dissociation period of 30 s after the first association.

PBMC isolation, cell freezing, and thawing

Fresh blood, buffy coats, or mononuclear blood cell concentrates were obtained from healthy volunteers at the Department of Immunology or from the ZKT Tübingen gGmbH. Participants gave informed consent and the studies were approved by the ethical review committee of the University of Tübingen, projects 156/2012B01 and 713/2018BO2. Blood products were diluted with PBS 1x (homemade from 10x stock solution, Lonza, Switzerland) and PBMCs were isolated by density gradient centrifugation with Biocoll separation solution (Biochrom, Germany). PBMCs were washed twice with PBS 1x, counted with a NC-250 cell counter (Chemometec, Denmark), and resuspended in heat-inactivated (h.i.) fetal bovine serum (Capricorn Scientific, Germany) containing 10% DMSO (Merck). Cells were immediately transferred into a -80°C freezer in a freezing container (Mr. Frosty; Thermo Fisher Scientific). After at least 24 hours, frozen cells were transferred into a liquid nitrogen tank and were kept

bioRxiv preprint doi: https://doi.org/10.1101/2021.07.02.450848; this version posted July 4, 2021. The copyright holder for this preprint (which was not certified by peer review) is the author/funder, who has granted bioRxiv a license to display the preprint in perpetuity. It is made available under aCC-BY-NC-ND 4.0 International license.

frozen until use. For the experiments, cells were thawed in IMDM (+L-Glutamin +25mM HEPES; Life Technologies) supplemented with 2.5% h.i. human serum (HS; PanBiotech, Germany), 1x P/S (Sigma-Aldrich), and 50 µm β-Mercaptoethanol (β-ME; Merck), washed once, counted and used for downstream assays.

Affinity determination by flow cytometry

For cell-based affinity determination, HEK293-hCD4 were detached using enzyme-free cell dissociation buffer (Gibco) and resuspended in FACS buffer (PBS containing 5% FBS). For each staining condition 200,000 cells were incubated with suitable dilution series of CD4 nanobodies at 4°C for 30 min. Cells were washed two times and for detection Cy5 AffiniPure Goat Anti-Alpaca IgG, VHH domain (Jackson ImmunoResearch) was applied for 15 min. PBMCs (Department of Immunology/ ZKT Tübingen gGmbH, Germany) were freshly thawed and resuspended in FACS buffer. For each sample 200,000 cells were incubated with suitable concentrations of CD4 Nbs coupled to CF568 in combination with 1:500 dilution of anti-CD3-FITC (BD Biosciences) at 4°C for 30 min. For control staining PE/Cy5-labeled anti-human CD4 antibody (RPA-T4, Biolegend) was used. After two washing steps, samples were resuspended in 200 µl FACS buffer and analyzed with a BD FACSMelody Cell Sorter. Final data analysis was performed via FlowJo10® software (BD Biosciences).

Sortase labeling of nanobodies

Sortase A pentamutant (eSrtA) in pET29 was a gift from David Liu (Addgene plasmid # 75144) and was expressed and purified as described (80). CF568-coupled peptide H-Gly-Gly-Gly-Doa-Lys-NH_2 (sortase substrate) was custom-synthesized by Intavis AG. For the click chemistry a peptide H-Gly-Gly-Gly-propyl-azide was synthesized. In brief, for sortase coupling 50 µM Nb, 250 µM sortase peptide dissolved in sortase buffer (50 mM Tris, pH 7.5, and 150 mM NaCl) and 10 µM sortase were mixed in coupling buffer (sortase buffer with 10 mM $CaCl_2$) and incubated for 4 h at 4°C. Uncoupled Nb and sortase were depleted by IMAC. Unbound excess of unreacted sortase peptide was removed using Zeba Spin Desalting Columns

bioRxiv preprint doi: https://doi.org/10.1101/2021.07.02.450848; this version posted July 4, 2021. The copyright holder for this preprint (which was not certified by peer review) is the author/funder, who has granted bioRxiv a license to display the preprint in perpetuity. It is made available under aCC-BY-NC-ND 4.0 International license.

(ThermoFisher Scientific, cat. #89890). Azide-coupled Nbs were labeled by SPAAC (strain-promoted azide-alkyne cycloaddition) click chemistry reaction with 2-fold molar excess of DBCO-Cy5.5 (Jena Bioscience) for 2 h at 25°C. Excess DBCO-Cy5.5 was subsequently removed by dialysis (GeBAflex-tube, 6-8 kDa, Scienova). Finally, to remove untagged Nb, (side product of the sortase reaction), we used hydrophobic interaction chromatography (HIC, HiTrap Butyl-S FF, Cytiva). Binding of DBCO-Cy5.5-coupled Nb occurred in 50 mM H_2NaPO_4, 1.5 M $(NH4)_2SO_4$, pH7.2. Elution took place with 50 mM H_2NaPO_4, pH7.2. Dye-labeled protein fractions were analyzed by SDS-PAGE followed by fluorescent scanning on a Typhoon Trio (GE-Healthcare, CF568: excitation 532 nm, emission filter settings 580 nm BP 30; Cy5.5 excitation 633 nm, emission filter settings 670 nm BP 30; 546) and subsequent Coomassie staining. Identity and purity of final products were determined by LC-MS (CD4-Nbs-CF568, >60%; CD4-Nb1-Cy5.5, ~94%; CD4-Nb4-Cy5.5, ~99%; GBP-Cy5.5; ~94%, CD4-Nb1-3, ~99%; bivGFP-Nb, ~99%).

Hydrogen-deuterium exchange

CD4 deuteration kinetics and epitope elucidation

On basis of the affinity constants of 5.1 nM (CD4-Nb1), 6.5 nM (CD4-Nb2), 75.3 nM (CD4-Nb3) (pre-determined by BLI analysis) the molar ratio of antigen to Nb was calculated ensuring 90% complex formation according to (81). CD4 (5 µL, 65.5 µM) was pre-incubated with CD4-specific Nbs (5 µl; 60.3; 67.4 and 143.1 µM for Nb1; Nb2 and Nb3 respectively) for 10 min at 25°C. Deuteration samples containing CD4 only were pre-incubated with PBS instead of the Nbs. HDX of the pre-incubated samples was initiated by 1:10 dilution with PBS (150 mM NaCl, pH7.4) prepared with D_2O leading to a final content of 90% D_2O. After 5 and 50 min incubation at 25°C, aliquots of 20 µL were taken and quenched by adding 20 µL ice-cold quenching solution (0.2 M TCEP with 1.5% formic acid and 4 M guanidine HCl in 100 mM ammonium formate solution pH2.2) resulting in a final pH of 2.5. Quenched samples were immediately snap-frozen.

bioRxiv preprint doi: https://doi.org/10.1101/2021.07.02.450848; this version posted July 4, 2021. The copyright holder for this preprint (which was not certified by peer review) is the author/funder, who has granted bioRxiv a license to display the preprint in perpetuity. It is made available under aCC-BY-NC-ND 4.0 International license.

Immobilized pepsin (TFS) was prepared using 60 µl of 50% slurry (in ammonium formate solution pH2.5) that was then dried by centrifugation (1000 x g for 3 min at 0°C) and discarding the supernatant. Prior each analysis, samples were thawed and added to the dried pepsin beads. After digestion for 2 min in a water ice bath the samples were separated by centrifugation at 1000 x g for 30 s at 0°C using a 22 µm filter (Merck, Millipore) and were immediately analyzed by LC-MS. Undeuterated control samples for each complex and CD4 alone were prepared under the same conditions using H_2O instead of D_2O. Additionally, each Nb was digested without addition of CD4 to generate a list of peptic peptides deriving from the Nb. The HDX experiments of the CD4-Nb-complex were performed in triplicates. The back-exchange of the method as determined using a standard peptide mixture of 14 synthetic peptides was 24%.

Chromatography and Mass Spectrometry

HDX samples were analyzed as described previously (78).

HDX data analysis

A peptic peptide list was generated in a preliminary LC-MS/MS experiment as described previously (78). For data based search no enzyme selectivity was applied, furthermore, identified peptides were manually evaluated to exclude peptides originated through cleavage after arginine, histidine, lysine, proline and the residue after proline (82). Additionally, a separate list of peptides for each nanobody was generated and peptides overlapping in mass, retention time and charge with the antigen digest, were manually removed. Analysis of the deuterated samples was performed in MS mode only and HDExaminer v2.5.0 (Sierra Analytics, USA) was used to calculate the deuterium uptake (centroid mass shift). HDX could be determined for peptides covering 87-88% of the CD4 sequence (**Supplementary Fig. 11**). The calculated percentage deuterium uptake of each peptide between CD4-Nb and CD4-only were compared. Any peptide with uptake reduction of 5% or greater upon Nb binding was

bioRxiv preprint doi: https://doi.org/10.1101/2021.07.02.450848; this version posted July 4, 2021. The copyright holder for this preprint (which was not certified by peer review) is the author/funder, who has granted bioRxiv a license to display the preprint in perpetuity. It is made available under aCC-BY-NC-ND 4.0 International license.

considered as protected. All relevant HDX parameters are shown in **Supplementary Table S3** as recommended (83).

Endotoxin determination and removal

The concentration of bacterial endotoxins was determined with Pierce LAL Chromogenic Endotoxin Quantitation Kit (Thermo Fisher Scientific) and removal occurred using EndoTrap HD 1 ml (Lionex) according to the manufacturers´ protocols.

Synthetic peptides

The following HLA-class II peptides were used for the stimulations: MHC class II pool (HCMVA pp65 aa 109-123 MSIYVYALPLKMLNI, HCMV pp65 aa 366-382 HPTFTSQYRIQGKLEYR, EBVB9 EBNA2 aa 276-290 PRSPTVFYNIPPMPL, EBVB9 EBNA1 aa 514-527 KTSLYNLRRGTALA, EBV BXLF2 aa 126-140 LEKQLFYYIGTMLPNTRPHS, EBV BRLF1 aa 119-133 DRFFIQAPSNRVMIP, EBVB9 EBNA3 aa 381-395 PIFIRRLHRLLLMRA, EBVB9 GP350 aa 167-181 STNITAVVRAQGLDV, IABAN HEMA aa 306-318 PKYVKQNTLKLAT,) or CMVpp65 aa 510-524 YQEFFWDANDIYRIF. All peptides were synthesized and dissolved in water 10% DMSO as previously described (purity ≥ 80%), and were kindly provided by S. Stevanović (84).

Stimulation and cultivation of PBMCs

PBMCs from donors previously screened for *ex vivo* $CD4^+$ T cell reactivities against MHC-class II peptides were thawed and rested in T cell medium (TCM; IMDM + 1x P/S + 50µM β-ME + 10% h.i. HS) containing 1µg/mL DNase I (Sigma-Aldrich) at a concentration of $2\text{-}3\times10^6$ cells/mL for 3h at 37°C and 7.5% CO_2. After resting, cells were washed once, counted and up to 1×10^8 cells were labeled with 1.5-2 µM Carboxyfluorescein succinimidyl ester (CFSE; BioLegend, USA) in 1 mL PBS 1X for 20 min according to the manufacturer's protocol. The cells were washed twice in medium containing 10% FBS after CFSE labeling and incubated with 5 µM, 0.5 µM, or 0.05 µM of CD4-Nb1, CD4-Nb4 or a control Nb for 1h at 37°C in serum-

bioRxiv preprint doi: https://doi.org/10.1101/2021.07.02.450848; this version posted July 4, 2021. The copyright holder for this preprint (which was not certified by peer review) is the author/funder, who has granted bioRxiv a license to display the preprint in perpetuity. It is made available under aCC-BY-NC-ND 4.0 International license.

free IMDM medium. Concentrations and duration were chosen to mimick the expected approximate concentration and serum retention time during clinical application. After incubation, cells were washed twice, counted and each condition was separated into three parts and seeded in a 48-well cell culture plate (1.6-2.5x10^6 cells/well in triplicates). Cells were stimulated with either 10 µg/ml PHA-L (Sigma-Aldrich), 5 µg/mL MHC class-II peptide(s) or left unstimulated, and cultured at 37°C and 7.5% CO_2. 2 ng/mL recombinant human IL-2 (R&D, USA) were added on days 3, 5, and 7. One third of the culture on day 4, one half of the culture on day 6 and day 8, and the remaining cells on day 12 were harvested, counted and stained for flow cytometry analyses. For donor 1, the proliferation/activation status and cytokine production were analyzed in two different experiments, whereas for donors 2 and 3, cells from a single experiment were used for the three assays.

Assessment of T cell proliferation and activation

Cells from days 4, 6, and 8 were transferred into a 96-well round-bottom plate and washed twice with FACS buffer (PBS + 0.02% sodium azide (Roth, Germany) +2 mM EDTA (Sigma-Aldrich) +2% h.i. FBS). Extracellular staining was performed with CD4 APC-Cy7 (RPA-T4, BD Biosciences), CD8 BV605 (RPA-T8, BioLegend), the dead cell marker Zombie Aqua (BioLegend), CD25 PE-Cy7 (BC96, BioLegend), CD69 PE (FN50, BD Biosciences) and incubated for 20 min at 4°C. All antibodies were used at pre-tested optimal concentrations. Cells were washed twice with FACS buffer. Approx. 500.000 cells were acquired on the same day using a LSRFortessaTM SORP (BD Biosciences, USA) equipped with the DIVA Software (Version 6, BD Biosciences, USA). The percentage of proliferating $CD4^+$ cells was determined by assessment of CFSE negative cells, activation by the percentage of $CD69^+$ or $CD25^+$.

Assessment of T cell function by intracellular cytokine staining

On day 12, the MHC class II peptide(s)-stimulated and cultured cells were transferred into a 96-well round-bottom plate (0.5 to 1x 10^6 cells/well) and restimulated using 10 µg/ml of the same peptide(s), 10 µg/ml Staphylococcus enterotoxin B (SEB, Sigma-Aldrich; positive

bioRxiv preprint doi: https://doi.org/10.1101/2021.07.02.450848; this version posted July 4, 2021. The copyright holder for this preprint (which was not certified by peer review) is the author/funder, who has granted bioRxiv a license to display the preprint in perpetuity. It is made available under aCC-BY-NC-ND 4.0 International license.

control), or 10% DMSO (negative control). Protein transport inhibitors Brefeldin A (10 µg/ml, Sigma-Aldrich) and Golgi Stop (BD Biosciences) were added at the same time as the stimuli. After 14 h stimulation at 37°C and 7.5% CO_2, cells were stained extracellularly with the fluorescently labeled antibodies CD4 APC-Cy7, CD8 BV605, and Zombie Aqua and incubated for 20 min at 4°C. After, cells were washed once, then fixed and permeabilized using the BD Cytofix/Cytoperm solution (BD Biosciences) according to the manufacturer's instructions, stained intracellularly with TNF Pacific Blue (Mab11), IL-2 PE-Cy7 (MQ1-17H12), IFN-γ AlexaFluor 700 (4S.B7) and CD154 APC (2431) antibodies (all BioLegend) (85) and washed twice. Approx. 500,000 cells were acquired on the same day using a LSRFortessaTM SORP (BD Biosciences, USA), equipped with the DIVA Software (Version 6, BD Biosciences). All flow cytometry analyses were performed with FlowJo version 10.6.2, gating strategies are shown in **Supplementary Fig. 6**. Statistical analyses were performed with GraphPad Prism version 9.0.0.

Full blood stimulation and cytokine release assay

100 µl of lithium-heparin blood was incubated for 1 h at 37°C and 7.5% CO_2. The blood was stimulated with 5 µM Nb (CD4-Nb1, CD4-Nb4 or control Nb), with 100 ng/mL LPS (Invivogen, USA), or with 2 µg/mL PHA-L in a final volume of 250 µl (serum-free IMDM medium), or left unstimulated for 24 h at 37°C and 7.5% CO_2. After two centrifugations, supernatant was collected without transferring erythrocytes. The supernatants were frozen at -80°C until cytokine measurements. Levels of IL-1β, IL-1Ra, IL-4, IL-6, IL-8, IL-10, IL-12p70, IL-13, GM-CSF, IFNγ, MCP-1, MIP-1β, TNFα and VEGF were determined using a set of in house developed Luminex-based sandwich immunoassays each consisting of commercially available capture and detection antibodies and calibrator proteins. All assays were thoroughly validated ahead of the study with respect to accuracy, precision, parallelism, robustness, specificity and sensitivity (86, 87). Samples were diluted at least 1:4 or higher. After incubation of the pre-diluted samples or calibrator protein with the capture coated microspheres, beads were washed and incubated with biotinylated detection antibodies. Streptavidin-phycoerythrin was

bioRxiv preprint doi: https://doi.org/10.1101/2021.07.02.450848; this version posted July 4, 2021. The copyright holder for this preprint (which was not certified by peer review) is the author/funder, who has granted bioRxiv a license to display the preprint in perpetuity. It is made available under aCC-BY-NC-ND 4.0 International license.

added after an additional washing step for visualization. For control purposes, calibrators and quality control samples were included on each microtiter plate. All measurements were performed on a Luminex FlexMap® 3D analyzer system, using Luminex xPONENT® 4.2 software (Luminex, USA). For data analysis MasterPlex QT, version 5.0 was employed. Standard curve and quality control samples were evaluated according to internal criteria adapted to the Westgard Rules (88) to ensure proper assay performance.

Analysis of cross-species reactivity binding to mouse CD4$^+$ cells by flow cytometry

Murine CD4$^+$ cells were isolated from spleen and lymph nodes of C57BL/6N mice by positive selection over CD4 magnetic microbeads (Miltenyi Biotech, Germany). Human CD4$^+$ cells were extracted from blood using StraightFrom® Whole Blood CD4 MicroBeads (Miltenyi Biotech). Single cell suspensions were incubated with 0.75 µg/ml of CD4-Nbs-Cy5.5 (~47 – 60 nM) or GFP-Nb-Cy5.5 (~51 nM) in 1% FPS/PBS at 4°C for 20 min and subsequently analyzed on a LSR-II cytometer (BD biosciences).

Optical Imaging of CD4-expressing HPB-ALL tumors

Human T cell leukemia HPB-ALL cells (German Collection of Microorganisms and Cell Cultures GmbH, DSMZ, Braunschweig, Germany) were cultured in RPMI-1640 supplemented with 10% FBS and 1% P/S. 10^7 HPB-ALL cells were injected *subcutaneously* in the right upper flank of 7-week-old NOD SCID gamma mice (NSG, NOD.Cg-*Prkdc*^{scid} *Il2rg*^{tm1Wjl}/SzJ, Charles River Laboratories, Sulzfeld, Germany) and tumor growth was monitored for 2-3 weeks. When tumors reached a diameter ~7 mm, 5 µg of CD4-Nbs-Cy5.5 or control Nb (GFP-Nb-Cy5.5) were administered into the tail vein of 2 mice each. Optical imaging (OI) was performed repetitively in short-term isoflurane anesthesia over a period of 24 h using the IVIS Spectrum In Vivo Imaging System (PerkinElmer, Waltham, MA, USA). Four days after the first Nb administration, the CD4-Nbs-Cy5.5 groups received the GFP-Nb-Cy5.5 (and vice versa) and tumor biodistribution was analyzed identically by OI over 24 h. After the last imaging time point, animals were sacrificed and tumors were explanted for *ex vivo* OI analysis. Data were analyzed

bioRxiv preprint doi: https://doi.org/10.1101/2021.07.02.450848; this version posted July 4, 2021. The copyright holder for this preprint (which was not certified by peer review) is the author/funder, who has granted bioRxiv a license to display the preprint in perpetuity. It is made available under aCC-BY-NC-ND 4.0 International license.

with Living Image 4.4 software (PerkinElmer). The fluorescence intensities were quantified by drawing regions of interest around the tumor borders and were expressed as average radiant efficiency (photons/s)/(µW/cm^2) subtracted by the background fluorescence signal before Nb injection to eliminate potential residual signal from the previous Nb application. All mouse experiments were performed according to the German Animal Protection Law and were approved by the local authorities (Regierungspräsidium Tübingen, R5/18).

Immunofluorescence staining of explanted xenograft tumors

Freshly frozen 5 µm sections of hCD4-Nb1-Cy5.5-containing mice tumors were analyzed using an LSM 800 laser scanning microscope (Zeiss). Afterwards the sections were fixed with perjodate-lysine-paraformaldehyde, blocked using donkey serum and stained with primary rabbit-anti-CD4 antibody (Cell Marque, USA). Bound antibody was visualized using donkey-anti-rabbit-Cy3 secondary antibody (Dianova, Germany). YO-PRO-1 (Invitrogen, USA) was used for nuclear staining. Acquired images of the same areas were manually overlaid.

Analyses and Statistics

Data analysis of the flow cytometry data was performed with the FlowJo Software Version 10.6.2 (FlowJo LLT, USA) and graph preparation and statistical analysis was performed using the GraphPad Prism Software (Version 8.3.0 or higher).

bioRxiv preprint doi: https://doi.org/10.1101/2021.07.02.450848; this version posted July 4, 2021. The copyright holder for this preprint (which was not certified by peer review) is the author/funder, who has granted bioRxiv a license to display the preprint in perpetuity. It is made available under aCC-BY-NC-ND 4.0 International license.

References

1. Delhalle S, Bode SFN, Balling R, Ollert M, & He FQ (2018) A roadmap towards personalized immunology. NPJ Syst Biol Appl 4:9.

2. Rossi JF, Ceballos P, & Lu ZY (2019) Immune precision medicine for cancer: a novel insight based on the efficiency of immune effector cells. Cancer Commun (Lond) 39(1):34.

3. Scheuenpflug J (2017) Precision Medicine in Oncology and Immuno-Oncology: Where We Stand and Where We're Headed. Biomed Hub 2(Suppl 1):79-86.

4. Sharma P & Allison JP (2015) The future of immune checkpoint therapy. Science 348(6230):56-61.

5. Baumeister SH, Freeman GJ, Dranoff G, & Sharpe AH (2016) Coinhibitory Pathways in Immunotherapy for Cancer. Annu Rev Immunol 34:539-573.

6. Larkin J, et al. (2015) Combined Nivolumab and Ipilimumab or Monotherapy in Untreated Melanoma. N Engl J Med 373(1):23-34.

7. Holzinger A, Barden M, & Abken H (2016) The growing world of CAR T cell trials: a systematic review. Cancer Immunol Immunother 65(12):1433-1450.

8. Levy M, Kolodziejczyk AA, Thaiss CA, & Elinav E (2017) Dysbiosis and the immune system. Nature Reviews Immunology 17(4):219-232.

9. Chitnis T (2007) The role of CD4 T cells in the pathogenesis of multiple sclerosis. Int Rev Neurobiol 79:43-72.

10. Goverman J (2009) Autoimmune T cell responses in the central nervous system. Nat Rev Immunol 9(6):393-407.

11. Becker W, et al. (1990) Imaging rheumatoid arthritis specifically with technetium 99m CD4-specific (T-helper lymphocytes) antibodies. Eur J Nucl Med 17(3-4):156-159.

12. Borst J, Ahrends T, Babala N, Melief CJM, & Kastenmuller W (2018) CD4(+) T cell help in cancer immunology and immunotherapy. Nat Rev Immunol 18(10):635-647.

13. Di Mascio M, et al. (2009) Noninvasive in vivo imaging of CD4 cells in simian-human immunodeficiency virus (SHIV)-infected nonhuman primates. Blood 114(2):328-337.

bioRxiv preprint doi: https://doi.org/10.1101/2021.07.02.450848; this version posted July 4, 2021. The copyright holder for this preprint (which was not certified by peer review) is the author/funder, who has granted bioRxiv a license to display the preprint in perpetuity. It is made available under aCC-BY-NC-ND 4.0 International license.

14. Byrareddy SN, et al. (2016) Sustained virologic control in SIV+ macaques after antiretroviral and alpha4beta7 antibody therapy. Science 354(6309):197-202.

15. Aubert RD, et al. (2011) Antigen-specific CD4 T-cell help rescues exhausted CD8 T cells during chronic viral infection. Proceedings of the National Academy of Sciences of the United States of America 108(52):21182-21187.

16. Penaloza-MacMaster P, et al. (2015) Vaccine-elicited CD4 T cells induce immunopathology after chronic LCMV infection. Science 347(6219):278-282.

17. Mousset CM, et al. (2019) Comprehensive Phenotyping of T Cells Using Flow Cytometry. Cytometry A 95(6):647-654.

18. Doan M, et al. (2018) Diagnostic Potential of Imaging Flow Cytometry. Trends Biotechnol 36(7):649-652.

19. Behbehani GK (2017) Applications of Mass Cytometry in Clinical Medicine: The Promise and Perils of Clinical CyTOF. Clin Lab Med 37(4):945-964.

20. Hartmann FJ, et al. (2019) Comprehensive Immune Monitoring of Clinical Trials to Advance Human Immunotherapy. Cell reports 28(3):819-831 e814.

21. Matos LL, Trufelli DC, de Matos MG, & da Silva Pinhal MA (2010) Immunohistochemistry as an important tool in biomarkers detection and clinical practice. Biomark Insights 5:9-20.

22. Tay RE, Richardson EK, & Toh HC (2021) Revisiting the role of CD4(+) T cells in cancer immunotherapy-new insights into old paradigms. Cancer Gene Ther 28(1-2):5-17.

23. Tavare R, et al. (2016) An Effective Immuno-PET Imaging Method to Monitor CD8-Dependent Responses to Immunotherapy. Cancer Res 76(1):73-82.

24. Rubin RH, Baltimore D, Chen BK, Wilkinson RA, & Fischman AJ (1996) In vivo tissue distribution of CD4 lymphocytes in mice determined by radioimmunoscintigraphy with an 111In-labeled anti-CD4 monoclonal antibody. Proceedings of the National Academy of Sciences of the United States of America 93(15):7460-7463.

25. Steinhoff K, et al. (2014) Visualizing inflammation activity in rheumatoid arthritis with Tc-99 m anti-CD4-mAb fragment scintigraphy. Nucl Med Biol 41(4):350-354.

bioRxiv preprint doi: https://doi.org/10.1101/2021.07.02.450848; this version posted July 4, 2021. The copyright holder for this preprint (which was not certified by peer review) is the author/funder, who has granted bioRxiv a license to display the preprint in perpetuity. It is made available under aCC-BY-NC-ND 4.0 International license.

26. Kanwar B, et al. (2008) In vivo imaging of mucosal CD4+ T cells using single photon emission computed tomography in a murine model of colitis. J Immunol Methods 329(1-2):21-30.

27. Dammes N & Peer D (2020) Monoclonal antibody-based molecular imaging strategies and theranostic opportunities. Theranostics 10(2):938-955.

28. Dialynas DP, et al. (1983) Characterization of the murine antigenic determinant, designated L3T4a, recognized by monoclonal antibody GK1.5: expression of L3T4a by functional T cell clones appears to correlate primarily with class II MHC antigen-reactivity. Immunol Rev 74:29-56.

29. Wilde DB, Marrack P, Kappler J, Dialynas DP, & Fitch FW (1983) Evidence implicating L3T4 in class II MHC antigen reactivity; monoclonal antibody GK1.5 (anti-L3T4a) blocks class II MHC antigen-specific proliferation, release of lymphokines, and binding by cloned murine helper T lymphocyte lines. Journal of immunology 131(5):2178-2183.

30. Haque S, Saizawa K, Rojo J, & Janeway CA, Jr. (1987) The influence of valence on the functional activities of monoclonal anti-L3T4 antibodies. Discrimination of signaling from other effects. Journal of immunology 139(10):3207-3212.

31. Freise AC, et al. (2017) ImmunoPET Imaging of Murine CD4(+) T Cells Using Anti-CD4 Cys-Diabody: Effects of Protein Dose on T Cell Function and Imaging. Mol Imaging Biol 19(4):599-609.

32. Hamers-Casterman C, et al. (1993) Naturally occurring antibodies devoid of light chains. Nature 363(6428):446-448.

33. Lecocq Q, et al. (2019) Theranostics in immuno-oncology using nanobody derivatives. Theranostics 9(25):7772-7791.

34. Muyldermans S (2013) Nanobodies: natural single-domain antibodies. Annual review of biochemistry 82:775-797.

35. Steeland S, Vandenbroucke RE, & Libert C (2016) Nanobodies as therapeutics: big opportunities for small antibodies. Drug Discov Today 21(7):1076-1113.

bioRxiv preprint doi: https://doi.org/10.1101/2021.07.02.450848; this version posted July 4, 2021. The copyright holder for this preprint (which was not certified by peer review) is the author/funder, who has granted bioRxiv a license to display the preprint in perpetuity. It is made available under aCC-BY-NC-ND 4.0 International license.

36. Muyldermans S, et al. (2009) Camelid immunoglobulins and nanobody technology. Vet Immunol Immunopathol 128(1-3):178-183.

37. Chakravarty R, Goel S, & Cai W (2014) Nanobody: the "magic bullet" for molecular imaging? Theranostics 4(4):386-398.

38. Yang EY & Shah K (2020) Nanobodies: Next Generation of Cancer Diagnostics and Therapeutics. Front Oncol 10:1182.

39. Chanier T & Chames P (2019) Nanobody Engineering: Toward Next Generation Immunotherapies and Immunoimaging of Cancer. Antibodies (Basel) 8(1).

40. Popp MWL & Ploegh HL (2011) Making and breaking peptide bonds: protein engineering using sortase. Angewandte Chemie International Edition 50(22):5024-5032.

41. Massa S, et al. (2016) Sortase A-mediated site-specific labeling of camelid single-domain antibody-fragments: a versatile strategy for multiple molecular imaging modalities. Contrast media & molecular imaging 11(5):328-339.

42. Virant D, et al. (2018) A peptide tag-specific nanobody enables high-quality labeling for dSTORM imaging. Nature communications 9(1):930.

43. Braun MB, et al. (2016) Peptides in headlock–a novel high-affinity and versatile peptide-binding nanobody for proteomics and microscopy. Scientific reports 6.

44. Masuda S, et al. (2009) Dual antitumor mechanisms of Notch signaling inhibitor in a T-cell acute lymphoblastic leukemia xenograft model. Cancer Sci 100(12):2444-2450.

45. Awad RM, De Vlaeminck Y, Maebe J, Goyvaerts C, & Breckpot K (2018) Turn Back the TIMe: Targeting Tumor Infiltrating Myeloid Cells to Revert Cancer Progression. Frontiers in immunology 9:1977.

46. Binnewies M, et al. (2018) Understanding the tumor immune microenvironment (TIME) for effective therapy. Nat Med 24(5):541-550.

47. Speiser DE, Ho PC, & Verdeil G (2016) Regulatory circuits of T cell function in cancer. Nat Rev Immunol 16(10):599-611.

48. Fridman WH, Pages F, Sautes-Fridman C, & Galon J (2012) The immune contexture in human tumours: impact on clinical outcome. Nat Rev Cancer 12(4):298-306.

bioRxiv preprint doi: https://doi.org/10.1101/2021.07.02.450848; this version posted July 4, 2021. The copyright holder for this preprint (which was not certified by peer review) is the author/funder, who has granted bioRxiv a license to display the preprint in perpetuity. It is made available under aCC-BY-NC-ND 4.0 International license.

49. Rudd CE, Trevillyan JM, Dasgupta JD, Wong LL, & Schlossman SF (1988) The CD4 receptor is complexed in detergent lysates to a protein-tyrosine kinase (pp58) from human T lymphocytes. Proceedings of the National Academy of Sciences of the United States of America 85(14):5190-5194.

50. Gonzalez H, Hagerling C, & Werb Z (2018) Roles of the immune system in cancer: from tumor initiation to metastatic progression. Genes Dev 32(19-20):1267-1284.

51. Topalian SL, Drake CG, & Pardoll DM (2015) Immune checkpoint blockade: a common denominator approach to cancer therapy. Cancer Cell 27(4):450-461.

52. Palucka AK & Coussens LM (2016) The Basis of Oncoimmunology. Cell 164(6):1233-1247.

53. Pardoll DM (2012) The blockade of immune checkpoints in cancer immunotherapy. Nat Rev Cancer 12(4):252-264.

54. Tavare R, et al. (2015) Immuno-PET of Murine T Cell Reconstitution Postadoptive Stem Cell Transplantation Using Anti-CD4 and Anti-CD8 Cys-Diabodies. J Nucl Med 56(8):1258-1264.

55. Li H, et al. (2021) Noninvasive Radionuclide Molecular Imaging of the CD4-Positive T Lymphocytes in Acute Cardiac Rejection. Mol Pharm 18(3):1317-1326.

56. Kristensen LK, et al. (2019) CD4(+) and CD8a(+) PET imaging predicts response to novel PD-1 checkpoint inhibitor: studies of Sym021 in syngeneic mouse cancer models. Theranostics 9(26):8221-8238.

57. Choy EH, et al. (2002) Repeat-cycle study of high-dose intravenous 4162W94 anti-CD4 humanized monoclonal antibody in rheumatoid arthritis. A randomized placebo-controlled trial. Rheumatology (Oxford) 41(10):1142-1148.

58. Moreland LW, et al. (1995) Double-blind, placebo-controlled multicenter trial using chimeric monoclonal anti-CD4 antibody, cM-T412, in rheumatoid arthritis patients receiving concomitant methotrexate. Arthritis Rheum 38(11):1581-1588.

59. Rashidian M, et al. (2017) Predicting the response to CTLA-4 blockade by longitudinal noninvasive monitoring of CD8 T cells. J Exp Med 214(8):2243-2255.

bioRxiv preprint doi: https://doi.org/10.1101/2021.07.02.450848; this version posted July 4, 2021. The copyright holder for this preprint (which was not certified by peer review) is the author/funder, who has granted bioRxiv a license to display the preprint in perpetuity. It is made available under aCC-BY-NC-ND 4.0 International license.

60. Huang L, et al. (2008) SPECT imaging with 99mTc-labeled EGFR-specific nanobody for in vivo monitoring of EGFR expression. Mol Imaging Biol 10(3):167-175.

61. Roovers RC, et al. (2007) Efficient inhibition of EGFR signaling and of tumour growth by antagonistic anti-EFGR Nanobodies. Cancer Immunol Immunother 56(3):303-317.

62. Evazalipour M, et al. (2014) Generation and characterization of nanobodies targeting PSMA for molecular imaging of prostate cancer. Contrast Media Mol Imaging 9(3):211-220.

63. Blykers A, et al. (2015) PET Imaging of Macrophage Mannose Receptor-Expressing Macrophages in Tumor Stroma Using 18F-Radiolabeled Camelid Single-Domain Antibody Fragments. J Nucl Med 56(8):1265-1271.

64. Bala G, et al. (2018) Evaluation of [(99m)Tc]Radiolabeled Macrophage Mannose Receptor-Specific Nanobodies for Targeting of Atherosclerotic Lesions in Mice. Mol Imaging Biol 20(2):260-267.

65. Jailkhani N, et al. (2019) Noninvasive imaging of tumor progression, metastasis, and fibrosis using a nanobody targeting the extracellular matrix. Proceedings of the National Academy of Sciences of the United States of America 116(28):14181-14190.

66. Bruni D, Angell HK, & Galon J (2020) The immune contexture and Immunoscore in cancer prognosis and therapeutic efficacy. Nat Rev Cancer 20(11):662-680.

67. Accogli T, Bruchard M, & Vegran F (2021) Modulation of CD4 T Cell Response According to Tumor Cytokine Microenvironment. Cancers 13(3).

68. Sakihama T, Smolyar A, & Reinherz EL (1995) Oligomerization of CD4 is required for stable binding to class II major histocompatibility complex proteins but not for interaction with human immunodeficiency virus gp120. Proceedings of the National Academy of Sciences of the United States of America 92(14):6444-6448.

69. Jonsson P, et al. (2016) Remarkably low affinity of CD4/peptide-major histocompatibility complex class II protein interactions. Proceedings of the National Academy of Sciences of the United States of America 113(20):5682-5687.

bioRxiv preprint doi: https://doi.org/10.1101/2021.07.02.450848; this version posted July 4, 2021. The copyright holder for this preprint (which was not certified by peer review) is the author/funder, who has granted bioRxiv a license to display the preprint in perpetuity. It is made available under aCC-BY-NC-ND 4.0 International license.

70. Cruikshank WW, Greenstein JL, Theodore AC, & Center DM (1991) Lymphocyte chemoattractant factor induces CD4-dependent intracytoplasmic signaling in lymphocytes. Journal of immunology 146(9):2928-2934.

71. Vignali DA & Vignali KM (1999) Profound enhancement of T cell activation mediated by the interaction between the TCR and the D3 domain of CD4. Journal of immunology 162(3):1431-1439.

72. Baldari CT, et al. (1995) Distinct signaling properties identify functionally different CD4 epitopes. Eur J Immunol 25(7):1843-1850.

73. Traenkle B, et al. (2015) Monitoring interactions and dynamics of endogenous beta-catenin with intracellular nanobodies in living cells. Molecular & cellular proteomics : MCP 14(3):707-723.

74. Maier J, Traenkle B, & Rothbauer U (2015) Real-time analysis of epithelial-mesenchymal transition using fluorescent single-domain antibodies. Scientific reports 5:13402.

75. Arbabi Ghahroudi M, Desmyter A, Wyns L, Hamers R, & Muyldermans S (1997) Selection and identification of single domain antibody fragments from camel heavy-chain antibodies. FEBS letters 414(3):521-526.

76. Rothbauer U, et al. (2008) A versatile nanotrap for biochemical and functional studies with fluorescent fusion proteins. Molecular & Cellular Proteomics 7(2):282-289.

77. Davies G, et al. (2017) Towards Translational ImmunoPET/MR Imaging of Invasive Pulmonary Aspergillosis: The Humanised Monoclonal Antibody JF5 Detects Aspergillus Lung Infections In Vivo. Theranostics 7(14):3398-3414.

78. Wagner TR, et al. (2021) NeutrobodyPlex-monitoring SARS-CoV-2 neutralizing immune responses using nanobodies. EMBO Rep 22(5):e52325.

79. Becker M, et al. (2021) Exploring beyond clinical routine SARS-CoV-2 serology using MultiCoV-Ab to evaluate endemic coronavirus cross-reactivity. Nature communications 12(1):1152.

bioRxiv preprint doi: https://doi.org/10.1101/2021.07.02.450848; this version posted July 4, 2021. The copyright holder for this preprint (which was not certified by peer review) is the author/funder, who has granted bioRxiv a license to display the preprint in perpetuity. It is made available under aCC-BY-NC-ND 4.0 International license.

80. Chen I, Dorr BM, & Liu DR (2011) A general strategy for the evolution of bond-forming enzymes using yeast display. Proceedings of the National Academy of Sciences of the United States of America 108(28):11399-11404.

81. Kochert BA, Iacob RE, Wales TE, Makriyannis A, & Engen JR (2018) Hydrogen-Deuterium Exchange Mass Spectrometry to Study Protein Complexes. Methods Mol Biol 1764:153-171.

82. Hamuro Y & Coales SJ (2018) Optimization of Feasibility Stage for Hydrogen/Deuterium Exchange Mass Spectrometry. J Am Soc Mass Spectrom 29(3):623-629.

83. Masson GR, et al. (2019) Recommendations for performing, interpreting and reporting hydrogen deuterium exchange mass spectrometry (HDX-MS) experiments. Nature methods 16(7):595-602.

84. Loffler MW, et al. (2019) A Non-interventional Clinical Trial Assessing Immune Responses After Radiofrequency Ablation of Liver Metastases From Colorectal Cancer. Frontiers in immunology 10:2526.

85. Widenmeyer M, et al. (2012) Promiscuous survivin peptide induces robust CD4+ T-cell responses in the majority of vaccinated cancer patients. International journal of cancer. Journal international du cancer 131(1):140-149.

86. EMEA (2013) Guideline on Bioanalytical Method Validation. European Medicines Agency; Comittee for Medicinal Products for Human Use (CHMP).

87. FDA (2018) Bioanalytical Method Validation: Guidance for Industry. U.S. Department of Health and Human Services, Food and Drug Administration, Center for Drug Evaluation and Research, Center for Veterinary Medicine.

88. Westgard JO, Barry PL, Hunt MR, & Groth T (1981) A multi-rule Shewhart chart for quality control in clinical chemistry. Clin Chem 27(3):493-501.

89. Wu H, Kwong PD, & Hendrickson WA (1997) Dimeric association and segmental variability in the structure of human CD4. Nature 387(6632):527-530.

bioRxiv preprint doi: https://doi.org/10.1101/2021.07.02.450848; this version posted July 4, 2021. The copyright holder for this preprint (which was not certified by peer review) is the author/funder, who has granted bioRxiv a license to display the preprint in perpetuity. It is made available under aCC-BY-NC-ND 4.0 International license.

Figures

Figure 1

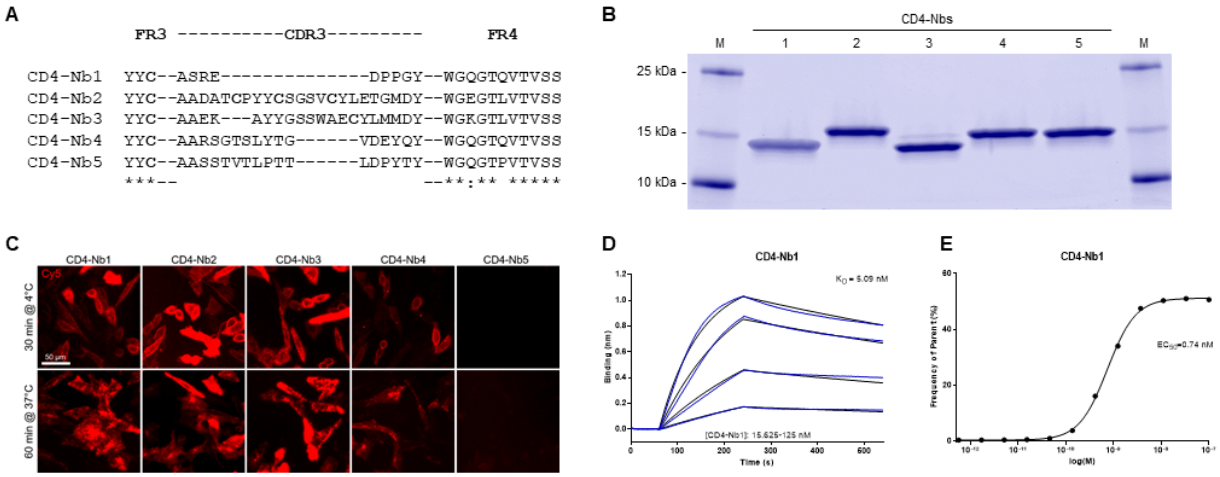

Table 1

	Dissociation constant K_D	k_{on} (10^5 M^{-1} s^{-1})	k_{off} (10^{-4} s^{-1})	R^2	EC_{50}
CD4-Nb1	5.1 nM	1.21 ± 0.022	6.13 ± 0.27	0.996	0.74 nM
CD4-Nb2	6.5 nM	1.22 ± 0.015	7.95 ± 0.18	0.998	0.73 nM
CD4-Nb3	75.3 nM	0.82 ± 0.026	61.8 ± 2.00	0.983	533 nM
CD4-Nb4	135 nM	1.18 ± 0.014	160 ± 0.97	0.998	7.36 µM

Figure 1 Identification and characterization of Nbs against hCD4

(**A**) Amino acid sequences of the complementarity determining region (CDR) 3 from unique CD4-Nbs selected after two rounds of biopanning are listed. (**B**) Recombinant expression and purification of CD4-Nbs using immobilized metal affinity chromatography (IMAC) and size exclusion chromatography (SEC). Coomassie stained SDS-PAGE of 2 µg of purified Nbs is shown. (**C**) Representative images of live CHO-hCD4 cells stained with CD4-Nbs for 30 min at 4°C (top row) or 60 min at 37°C (bottom row), scale bar: 50 µm. (**D**) For biolayer interferometry (BLI)-based affinity measurements, biotinylated hCD4 was immobilized on streptavidin biosensors. Kinetic measurements were performed using four concentrations of purified Nbs ranging from 15.6 nM - 1000 nM. As an example, the sensogram of CD4-Nb1 at indicated concentrations is shown. (**E**) EC_{50} determination by flow cytometry. Exemplarily shown for CD4-Nb1, the percentage of positively stained HEK293-hCD4 (frequency of parent) was plotted against indicated concentrations of CD4-Nbs.

Table 1 Summary of affinities (K_D), association (K_{on}) and dissociation constants (K_{off}) determined by BLI (left side) and EC_{50} values of flow cytometry (right side).

bioRxiv preprint doi: https://doi.org/10.1101/2021.07.02.450848; this version posted July 4, 2021. The copyright holder for this preprint (which was not certified by peer review) is the author/funder, who has granted bioRxiv a license to display the preprint in perpetuity. It is made available under aCC-BY-NC-ND 4.0 International license.

Figure 2

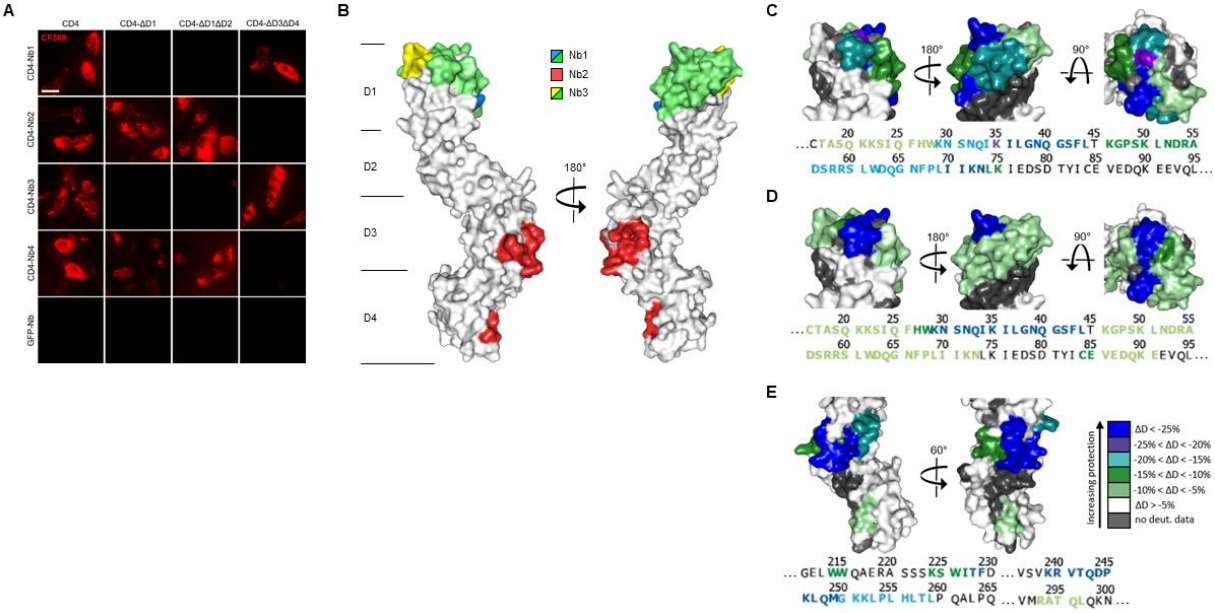

Figure 2 Localization of CD4-Nb binding epitopes

(**A**) Representative images of live CHO cells expressing full-length or domain-deletion mutants of hCD4 stained with fluorescently labeled CD4-Nbs (CF568) are shown, Scale bar 10 µm. (**B**) Surface structure model of hCD4 (PDBe 1wiq) (89) and the HDX-MS epitope mapping results of CD4-Nb1 – 3 are depicted. Different colours highlight the amino acid residues protected by CD4-Nb1 (blue), CD4-Nb2 (red) or CD4-Nb 3 (yellow). Overlapping residues protected by both Nb1 and Nb3, are coloured in green. A more detailed surface map (%ΔD) of these specific regions is highlighted in in **C** (CD4-Nb1), **D** (CD4-Nb3) and **E** (CD4-Nb2) with the corresponding CD4 amino acid sequence.

bioRxiv preprint doi: https://doi.org/10.1101/2021.07.02.450848; this version posted July 4, 2021. The copyright holder for this preprint (which was not certified by peer review) is the author/funder, who has granted bioRxiv a license to display the preprint in perpetuity. It is made available under aCC-BY-NC-ND 4.0 International license.

1016 **Figure 3**

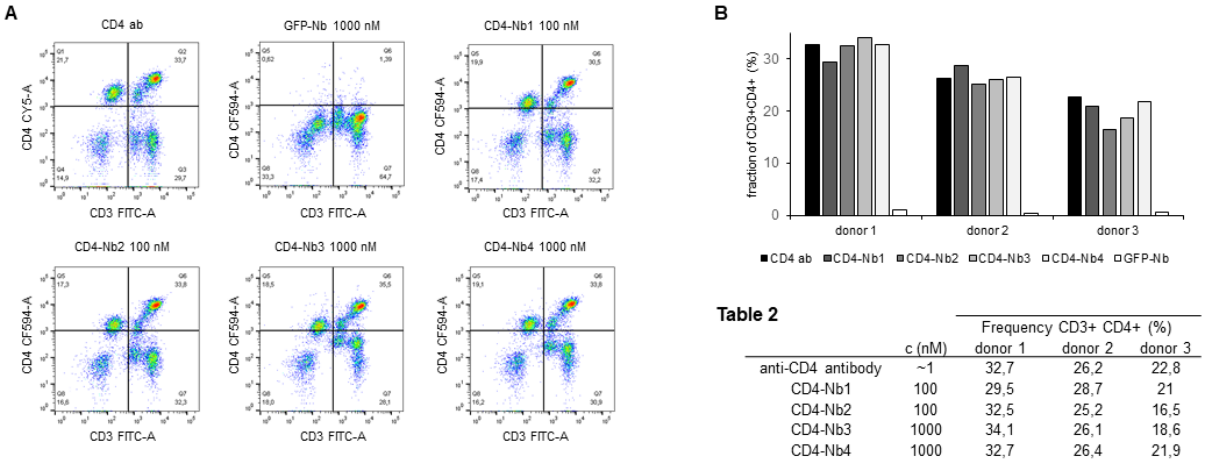

Table 2

		Frequency CD3+ CD4+ (%)		
	c (nM)	donor 1	donor 2	donor 3
anti-CD4 antibody	~1	32,7	26,2	22,8
CD4-Nb1	100	29,5	28,7	21
CD4-Nb2	100	32,5	25,2	16,5
CD4-Nb3	1000	34,1	26,1	18,6
CD4-Nb4	1000	32,7	26,4	21,9
GFP-Nb	1000	1,02	0,28	0,64

1017

1018

1019 **Figure 3 Flow cytometry analysis of human PBMCs stained with fluorescently labeled**

1020 **CD4-Nbs**

1021 (**A**) Schematic representation of the final gating step for $CD3^{+}CD4^{+}$ double-positive cells

1022 derived from donor one. (**B**) Percentage of double-positive cells of three donors, stained with

1023 CD4-Nb1 or CD4-Nb2 (100 nM), or CD4-Nb3 or CD4-Nb4 (1000 nM), compared to anti-CD4

1024 antibody and negative control Nb (GFP-Nb, 1000 nM).

1025 **Table 2** Percentage of double-positive PBMCs from three donors stained with hCD4-Nbs at

1026 indicated concentrations.

1027

1028

bioRxiv preprint doi: https://doi.org/10.1101/2021.07.02.450848; this version posted July 4, 2021. The copyright holder for this preprint (which was not certified by peer review) is the author/funder, who has granted bioRxiv a license to display the preprint in perpetuity. It is made available under aCC-BY-NC-ND 4.0 International license.

Figure 4

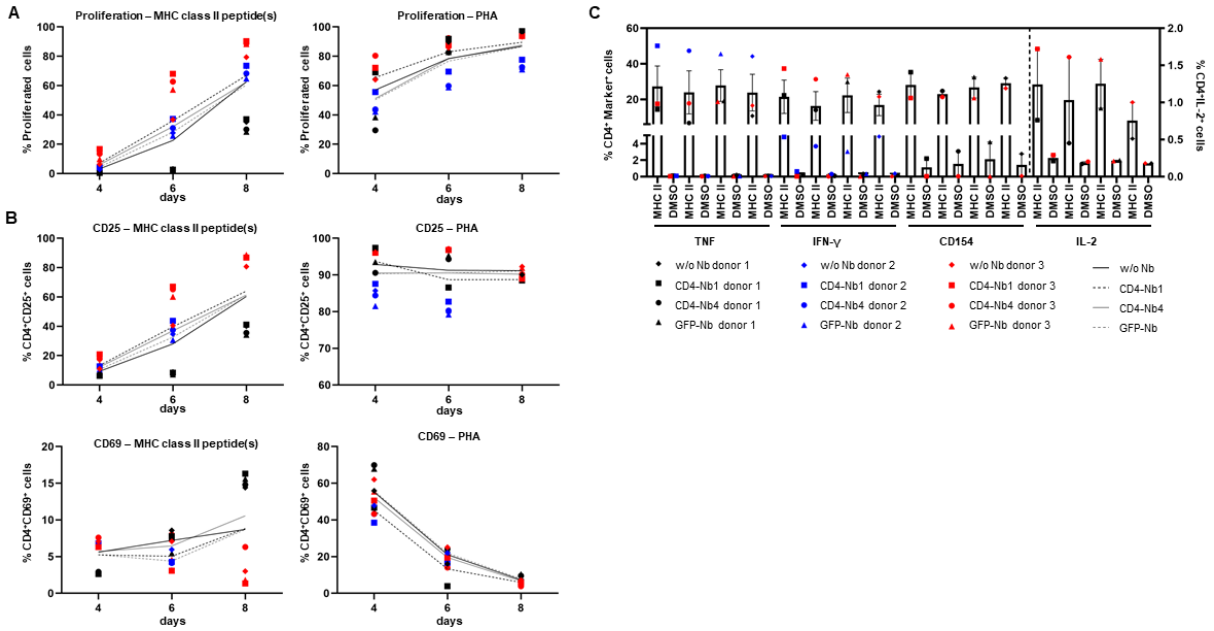

Figure 4 Impact of CD4-Nbs on activation, proliferation and cytokine release of T cells

Cells were stained with CFSE, treated with 5 µM Nbs or without for 1 h (one replicate each), washed and then stimulated with 5 µg/ml MHC-class II peptides, 10 µg/ml PHA or not stimulated, and cultured for 12 days. (**A**) Cells were analyzed by flow cytometry for proliferation (CFSE-low/negative fraction) and activation (CD25 and CD69) on days 4, 6, 8. Proliferation of $CD4^+$ cells after stimulation with MHC-class II peptide(s) (left) or PHA (right). (**B**) Activation markers on $CD4^+$ cells, Top: CD25 expression after stimulation with MHCII peptide(s) (left) or PHA (right); Bottom: CD69 expression after stimulation with MHCII peptide(s) (left) or PHA (right). Mean percentages of all 3 donors are shown as plain or dotted lines. (**C**) Cytokine and activation marker expression of $CD4^+$ cells – TNF, IFN-γ, CD154 (left y-axis) or IL-2 (right y-axis). Cells were restimulated on day 12 with MHC-class II peptide(s) or DMSO (background) for 14 h in the presence of Golgi Stop and Brefeldin A and analyzed by flow cytometry. Error bars display SEM. Gating strategy is shown in **Supplementary Fig. 6**, all percentages are given within $CD4^+$ T cells.

bioRxiv preprint doi: https://doi.org/10.1101/2021.07.02.450848; this version posted July 4, 2021. The copyright holder for this preprint (which was not certified by peer review) is the author/funder, who has granted bioRxiv a license to display the preprint in perpetuity. It is made available under aCC-BY-NC-ND 4.0 International license.

Figure 5

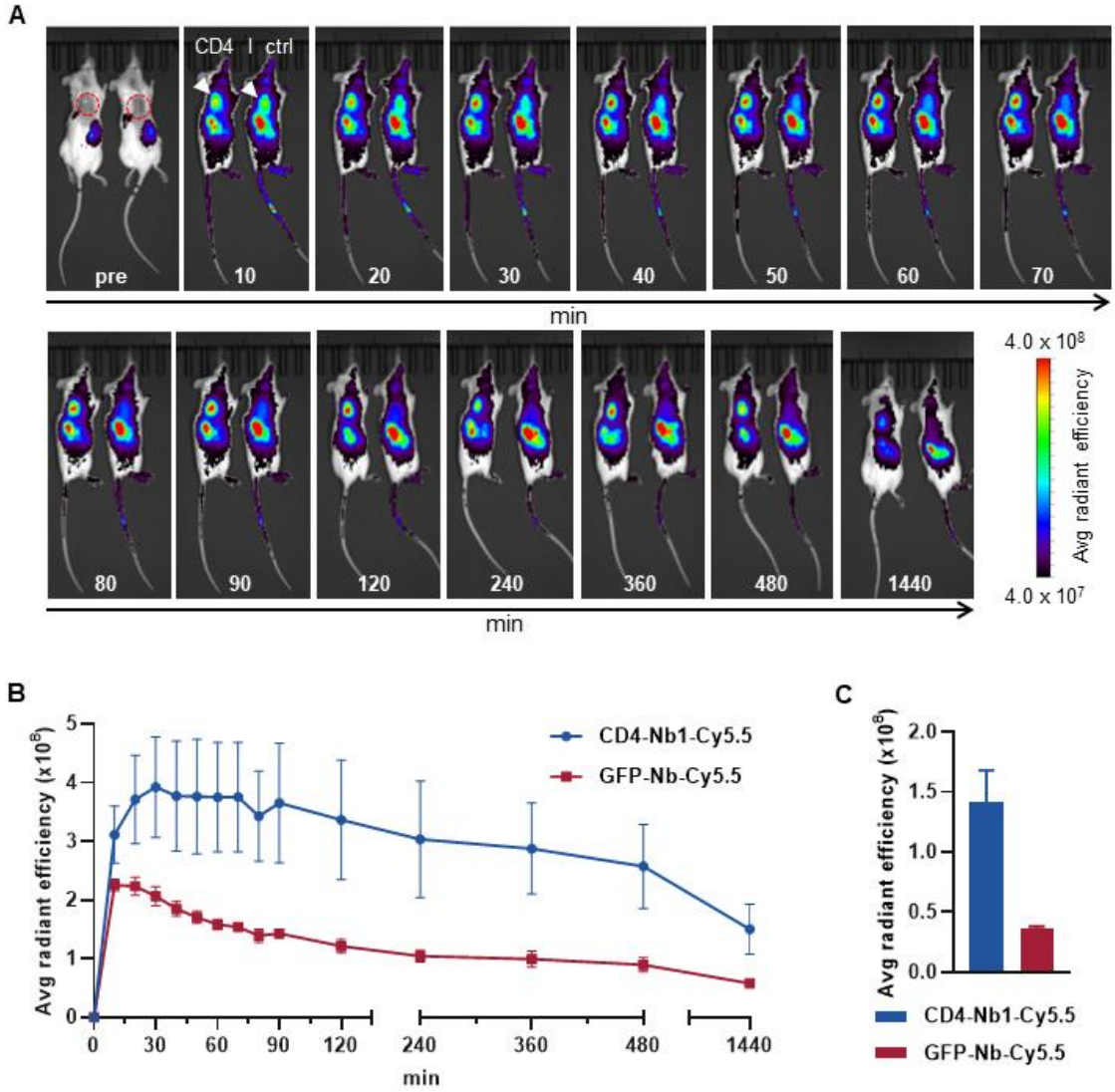

Figure 5 *In vivo* optical imaging (OI) of CD4-Nb1-Cy5.5

5 µg of CD4-Nb1-Cy5.5 or GFP-Nb-Cy5.5 were administered *i.v.* to *subcutaneously* human $CD4^+$ HPB-ALL-bearing NSG mice and tumor biodistribution was monitored by repetitive OI measurements over the course of 24 h. (**A**) Acquired images of each measurement time point of one representative mouse injected with CD4-Nb1-Cy5.5 (left, CD4) or GFP-Nb-Cy5.5 (right, ctrl). Red circles and white arrows indicate the tumor localization at the right upper flank. (**B**) Quantification of the fluorescence signal from the tumors (n = 4 per group, arithmetic mean of the average radiant efficiency ± SEM). (**C**) After the last imaging time point tumors were explanted for *ex vivo* OI, confirming increased accumulation of CD4-Nb1-Cy5.5 compared to the GFP-Nb-Cy5.5 (n = 2 per group, arithmetic mean ± SEM).

bioRxiv preprint doi: https://doi.org/10.1101/2021.07.02.450848; this version posted July 4, 2021. The copyright holder for this preprint (which was not certified by peer review) is the author/funder, who has granted bioRxiv a license to display the preprint in perpetuity. It is made available under aCC-BY-NC-ND 4.0 International license.

Supplementary Information

Supplementary Figure 1

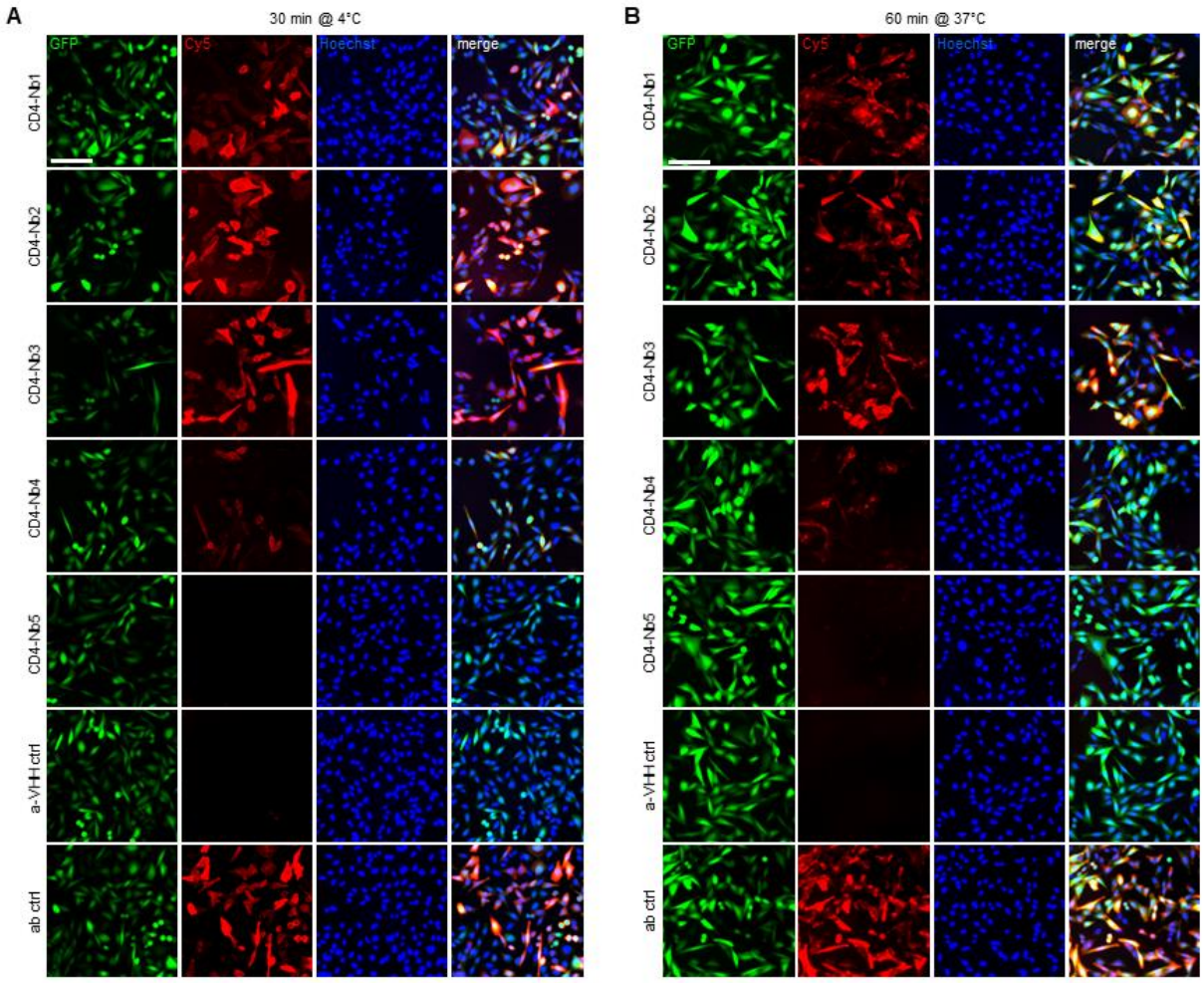

Supplementary Figure 1 Live-cell immunofluorescence staining of CHO-hCD4 cells incubated with CD4-Nbs (100 nM) followed by detection using a secondary Cy5-labeled anti-VHH antibody and 2 µg/ml Hoechst33258 for 30 min at 4°C (**A**) or 60 min at 37°C (**B**). Shown are representative images of CHO-hCD4 cells simultaneously expressing cytosolic GFP (left column) and hCD4 (second column from left) from a bicistronic mRNA. Nuclear staining and merge of channels is shown in column 3 and 4 from the left. Negative control staining using secondary Cy5-labeled anti-VHH antibody alone (a-VHH ctrl) and positive control using Cy5-labeled anti-hCD4 antibody (ab ctrl) are shown in bottom two rows. Scale bar 100 µm.

bioRxiv preprint doi: https://doi.org/10.1101/2021.07.02.450848; this version posted July 4, 2021. The copyright holder for this preprint (which was not certified by peer review) is the author/funder, who has granted bioRxiv a license to display the preprint in perpetuity. It is made available under aCC-BY-NC-ND 4.0 International license.

Supplementary Figure 2

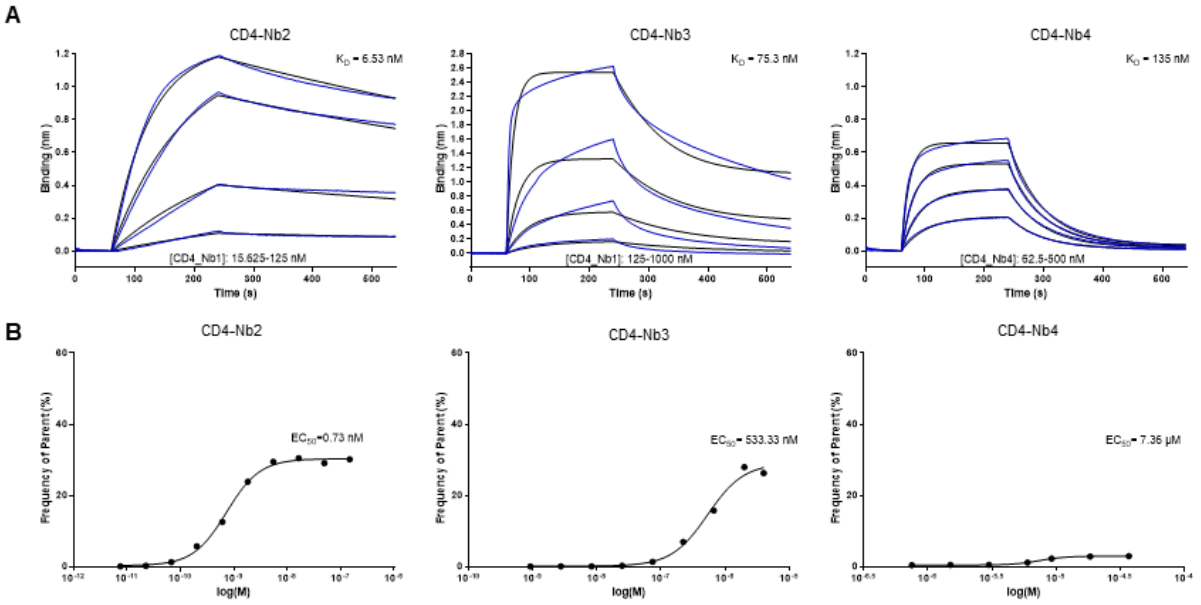

Supplementary Figure 2 Affinities of identified CD4-Nbs (**A**) Sensograms of biolayer interferometry-based affinity measurements of CD4-Nb2, CD4-Nb3 and CD4-Nb4 are shown. Biotinylated hCD4 was immobilized on streptavidin biosensors and kinetic measurements were performed by using four concentrations of purified Nbs ranging from 15.6 nM - 1 µM. (**B**) EC_{50} determination of CD4-Nbs for cellularly expressed hCD4 by flow cytometry. The percentage of positively stained HEK293-hCD4 (frequency of parent) was plotted against indicated concentrations of CD4-Nbs. EC_{50} values were calculated from a four-parametric sigmoidal model.

bioRxiv preprint doi: https://doi.org/10.1101/2021.07.02.450848; this version posted July 4, 2021. The copyright holder for this preprint (which was not certified by peer review) is the author/funder, who has granted bioRxiv a license to display the preprint in perpetuity. It is made available under aCC-BY-NC-ND 4.0 International license.

Supplementary Figure 3

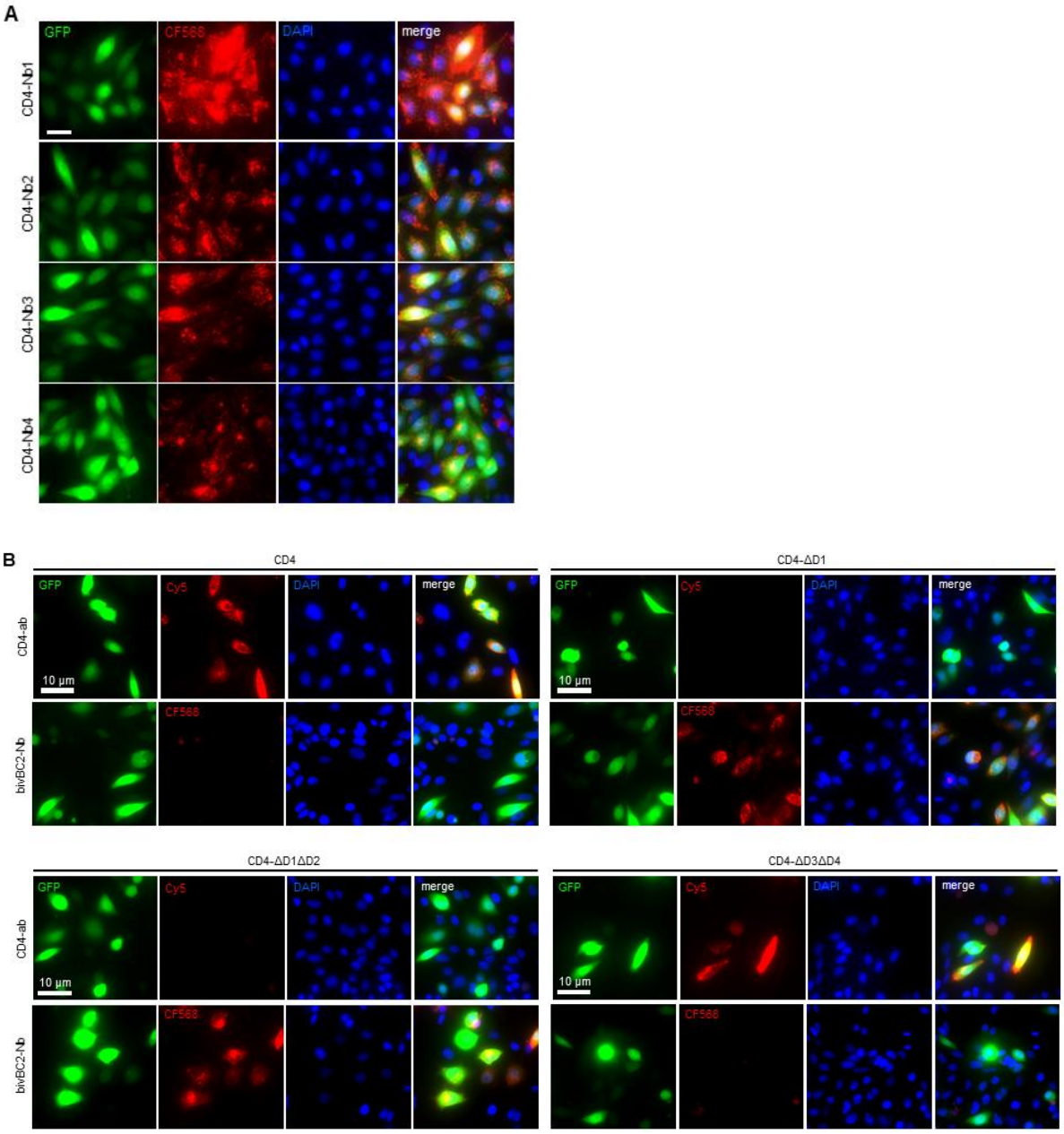

bioRxiv preprint doi: https://doi.org/10.1101/2021.07.02.450848; this version posted July 4, 2021. The copyright holder for this preprint (which was not certified by peer review) is the author/funder, who has granted bioRxiv a license to display the preprint in perpetuity. It is made available under aCC-BY-NC-ND 4.0 International license.

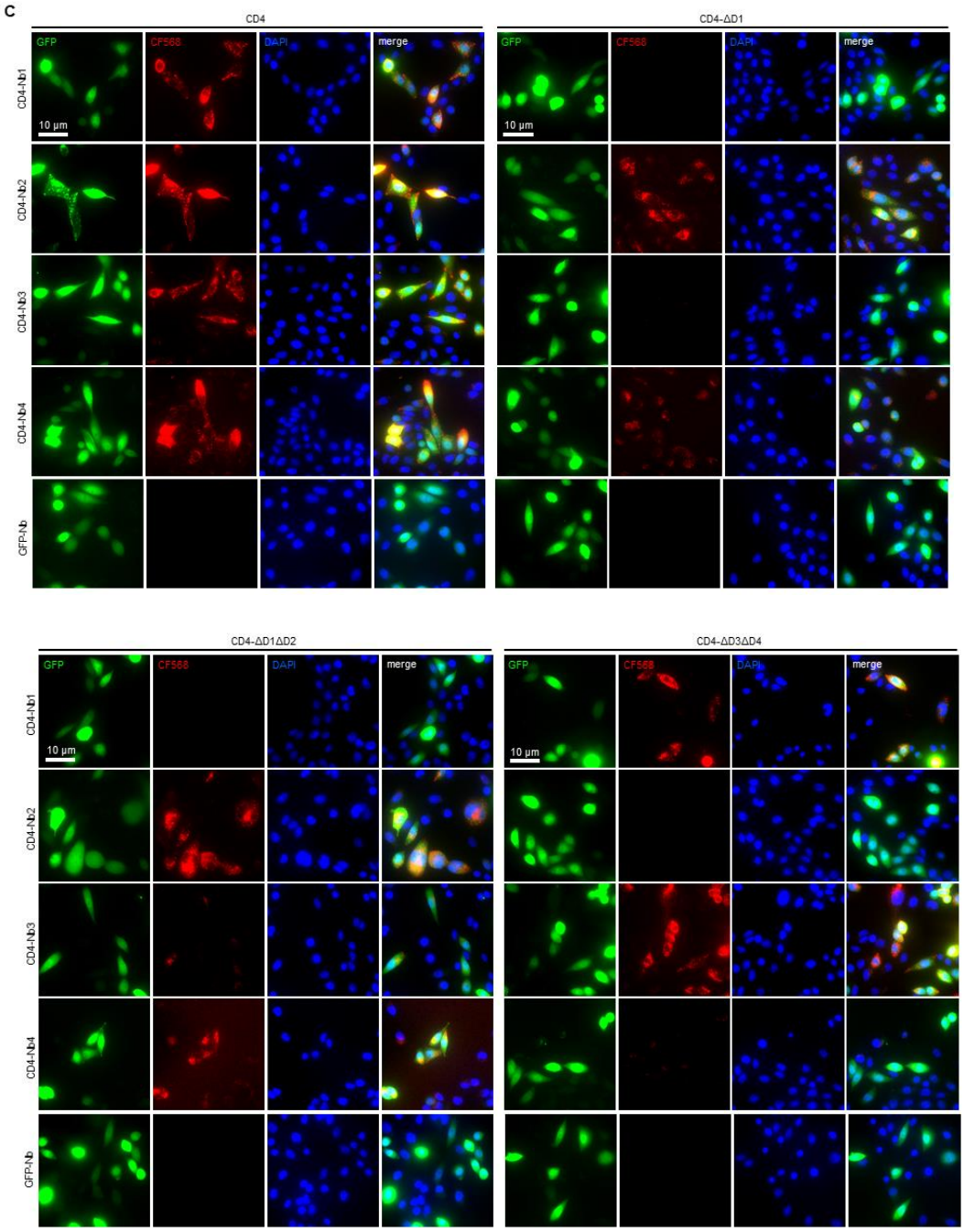

Supplementary Figure 3 CD4-Nbs bind different domains of human CD4. (**A**) Live-cell immunofluorescence staining of CHO-hCD4 cells with CD4-Nbs coupled to the fluorescent dye CF568, and 2 µg/ml Hoechst33258 for 60 min at 37°C. (**B**) Control staining of full-length hCD4 (CD4) or hCD4 domain-deletion mutants CD4-ΔD1, CD4-ΔD1ΔD2 or CD4-ΔD3ΔD4 with fluorescently labeled anti-CD4 antibody RPA-T4-PE/Cy5 (CD4-ab) or bivalent BC2-Nb coupled to CF568 (bivBC2-Nb). (**C**) Live-cell immunofluorescence staining of CHO cells transiently expressing full-length hCD4 or hCD4 domain-deletion mutants with CF568-labeled CD4-Nbs or a non-specific GFP-Nb (100 nM). Scale bars 10 µm.

bioRxiv preprint doi: https://doi.org/10.1101/2021.07.02.450848; this version posted July 4, 2021. The copyright holder for this preprint (which was not certified by peer review) is the author/funder, who has granted bioRxiv a license to display the preprint in perpetuity. It is made available under aCC-BY-NC-ND 4.0 International license.

Supplementary Figure 4

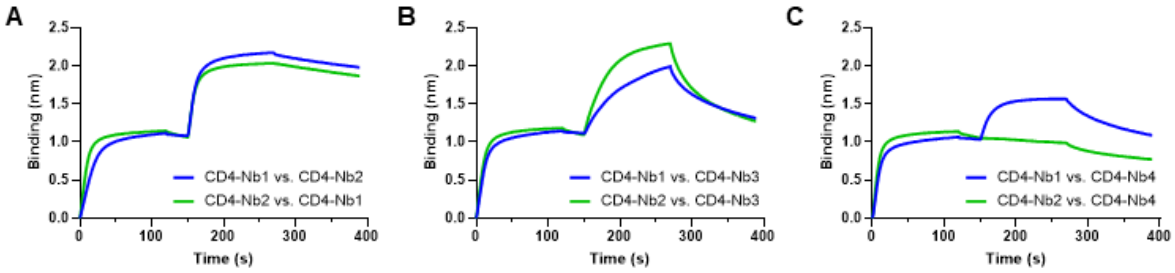

Supplementary Figure 4 Epitope binning analysis of CD4-Nbs by biolayer interferometry (BLI) (**A**) Representative BLI sensograms of single measurements of combinatorial Nb binding to the recombinant extracellular portion of hCD4 of CD4-Nb1 (blue) and CD4-Nb2 (green) with (**A**) one another, (**B**) CD4-Nb3, or (**C**) CD4-Nb4.

bioRxiv preprint doi: https://doi.org/10.1101/2021.07.02.450848; this version posted July 4, 2021. The copyright holder for this preprint (which was not certified by peer review) is the author/funder, who has granted bioRxiv a license to display the preprint in perpetuity. It is made available under aCC-BY-NC-ND 4.0 International license.

Supplementary Figure 5

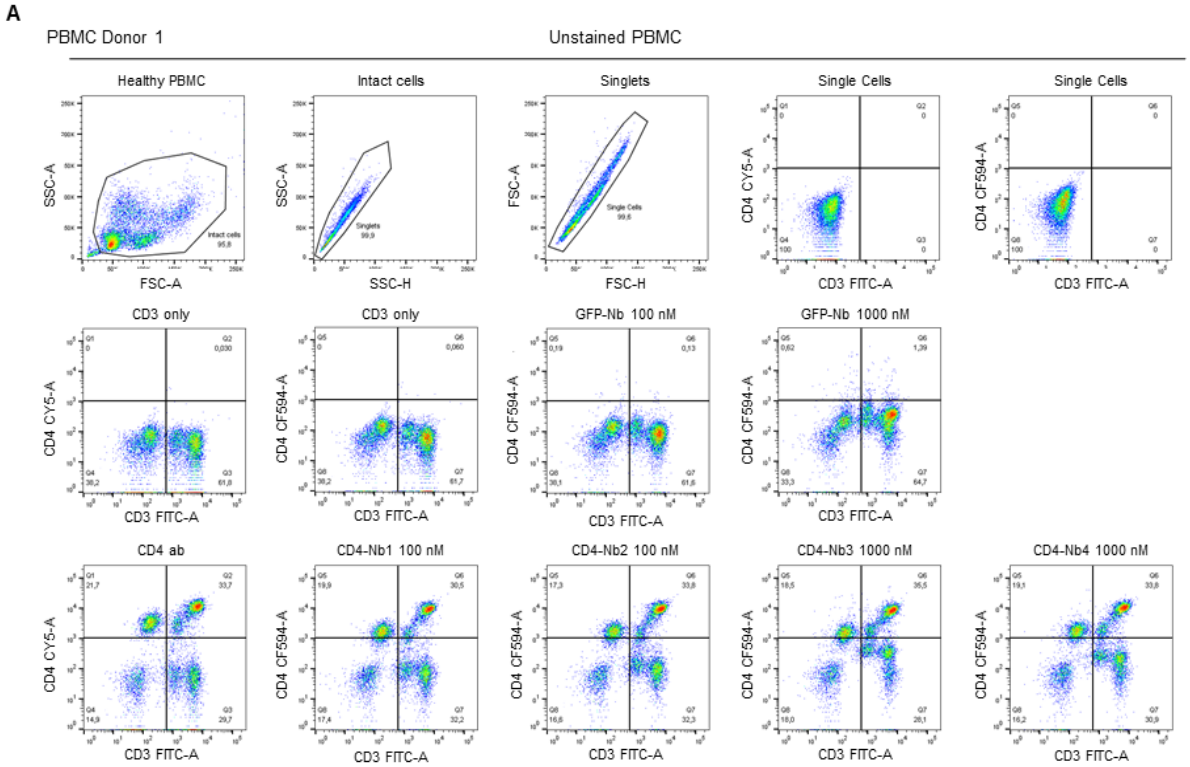

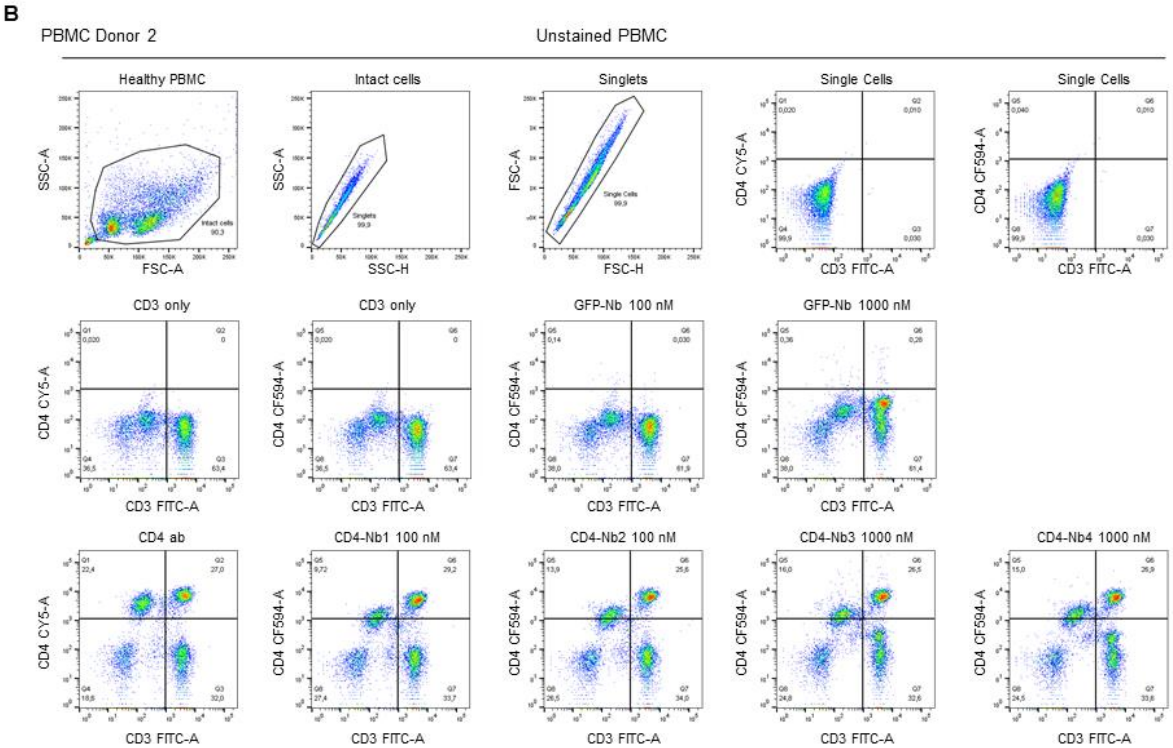

bioRxiv preprint doi: https://doi.org/10.1101/2021.07.02.450848; this version posted July 4, 2021. The copyright holder for this preprint (which was not certified by peer review) is the author/funder, who has granted bioRxiv a license to display the preprint in perpetuity. It is made available under aCC-BY-NC-ND 4.0 International license.

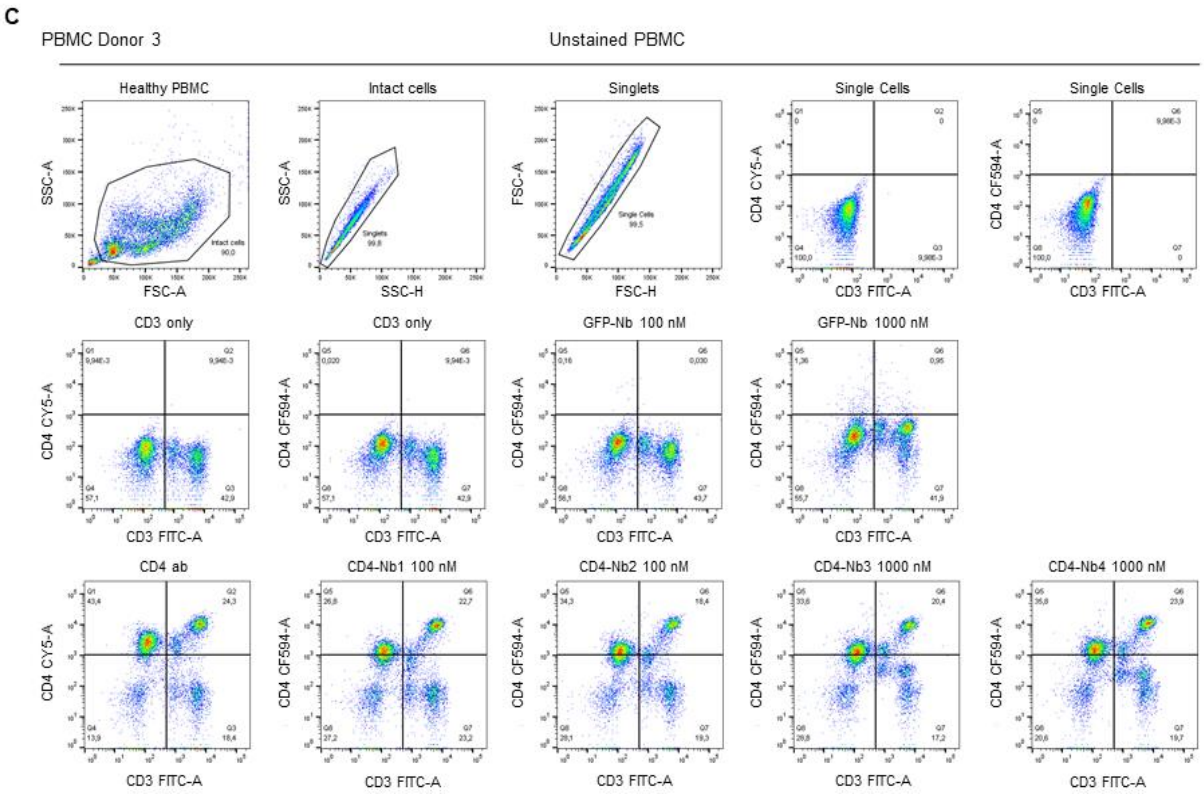

Supplementary Figure 5 Binding of CD4-Nbs to CD4$^+$ cells present in human PBMCs. Top row shows gating strategy for flow cytometry analysis of CD4$^+$CD3$^+$ double-positive human PBMCs. Middle and bottom row shows final gating step and quantification of these cells for donor 1 (**A**), donor 2 (**B**), and donor 3 (**C**) stained with an anti-CD4 antibody (CD4 ab), anti-GFP control Nb (GFP-Nb), or CD4-Nb1 - CD4-Nb4 at indicated concentrations.

bioRxiv preprint doi: https://doi.org/10.1101/2021.07.02.450848; this version posted July 4, 2021. The copyright holder for this preprint (which was not certified by peer review) is the author/funder, who has granted bioRxiv a license to display the preprint in perpetuity. It is made available under aCC-BY-NC-ND 4.0 International license.

Supplementary Figure 6

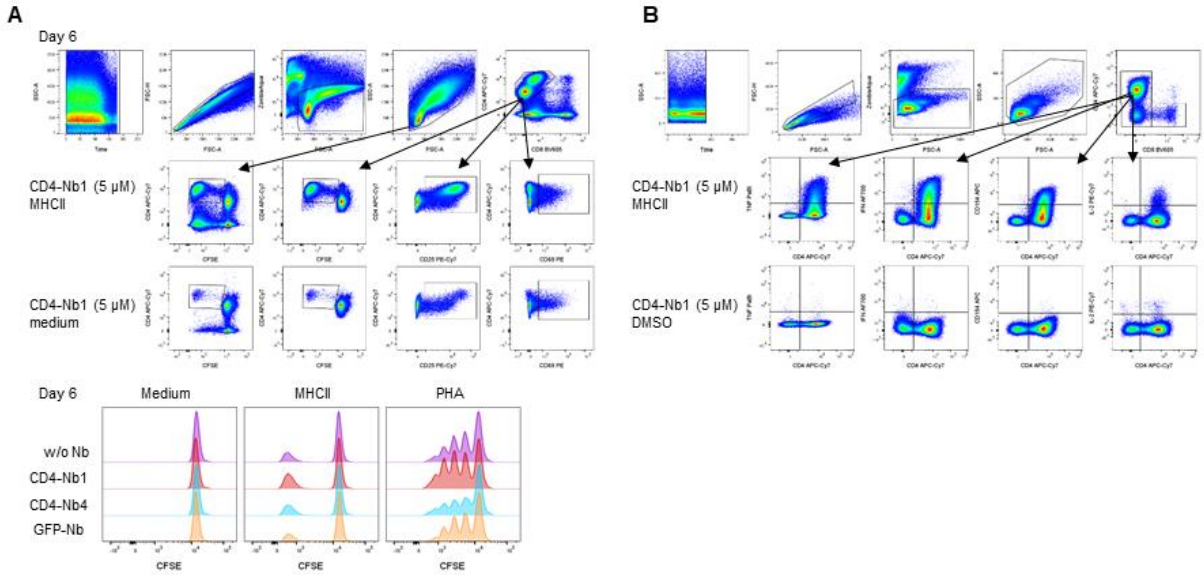

Supplementary Fig. 6 Determination of the effect of CD4-Nbs on CD4$^+$ T cells. (**A**) Gating strategy for analysis of proliferation and activation of CD4$^+$ cells after stimulation. Top row from left to right: Time gate, single cells, live cells, lymphocytes, CD4$^+$ cells. Middle and bottom rows: gates were place on proliferating CFSE-low/negative CD4$^+$ cells (left), CD25$^+$CD4$^+$ cells (middle) and CD69$^+$CD4$^+$ cells (right). Histogram overlay shows the number of divisions as CFSE labeling within CD4$^+$ cells. Shown is one representative example (donor 2) on day 6. (**B**) Gating strategy (donor 3) for analysis of activation marker and cytokine expression of CD4$^+$ cells in intracellular staining after 12 days of culture and 14 h restimulation. Top row from left to right: Time gate, single cells, live cells, lymphocytes, CD4$^+$ cells, CD4/CD8 staining (gating on CD8^{neg} cells). Middle and bottom rows show the expression of TNF, IFN-γ, CD154 and IL-2 after restimulation with MHC-class II peptides or control DMSO/water.

bioRxiv preprint doi: https://doi.org/10.1101/2021.07.02.450848; this version posted July 4, 2021. The copyright holder for this preprint (which was not certified by peer review) is the author/funder, who has granted bioRxiv a license to display the preprint in perpetuity. It is made available under aCC-BY-NC-ND 4.0 International license.

Supplementary Figure 7

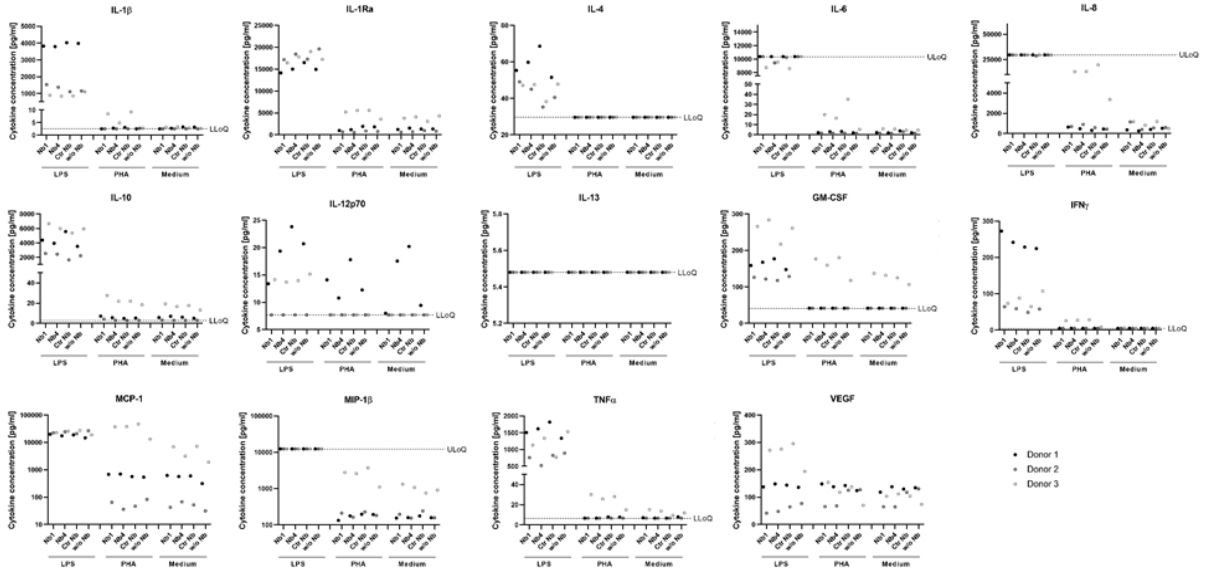

Supplementary Figure 7 Determination of cytokines secreted from whole blood samples of donors after treatment with CD4-Nbs. Blood samples of three donors were incubated with 5 µM CD4-Nb1, CD4-Nb4, GFP-Nb (control) or w/o Nb and stimulated with lipopolysaccharide (LPS), phytohaemagglutinin (PHA) or medium only as control. Secreted cytokines (listed in table S2) were measured and quantified using an in-house developed microsphere-based (Luminex) multiplex sandwich immunoassay. Results of one biological experiment are shown as colored dots indicating measured cytokine levels of one individual.

bioRxiv preprint doi: https://doi.org/10.1101/2021.07.02.450848; this version posted July 4, 2021. The copyright holder for this preprint (which was not certified by peer review) is the author/funder, who has granted bioRxiv a license to display the preprint in perpetuity. It is made available under aCC-BY-NC-ND 4.0 International license.

1135 **Supplementary Figure 8**

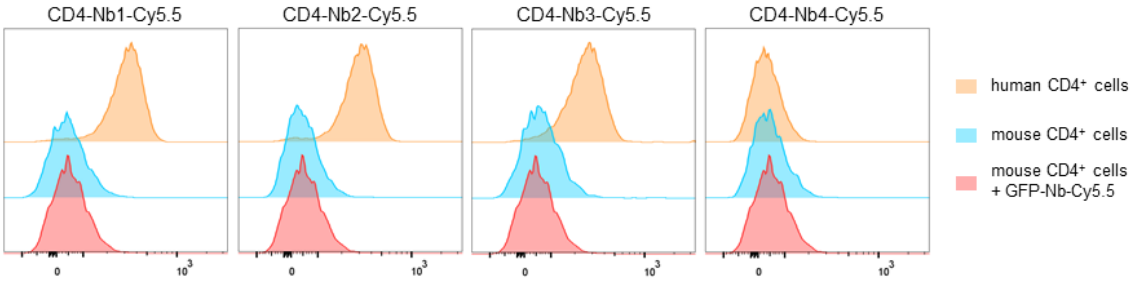

1136

1137 **Supplementary Figure 8** Cross-species reactivity testing of Cy5.5-labeled CD4-Nbs. Flow
1138 cytometry of human and mouse CD4$^+$ cells stained with CD4-Nbs-Cy5.5 or GFP-Nb-Cy5.5.
1139 Binding to human CD4 was confirmed for CD4-Nb1, CD4-Nb2 and CD4-Nb3. CD4-Nb4 did not
1140 show staining at this concentration (0.75 µg/ml, ~49 nM). None of the tested CD4-Nbs stained
1141 murine CD4.

1142

bioRxiv preprint doi: https://doi.org/10.1101/2021.07.02.450848; this version posted July 4, 2021. The copyright holder for this preprint (which was not certified by peer review) is the author/funder, who has granted bioRxiv a license to display the preprint in perpetuity. It is made available under aCC-BY-NC-ND 4.0 International license.

Supplementary Figure 9

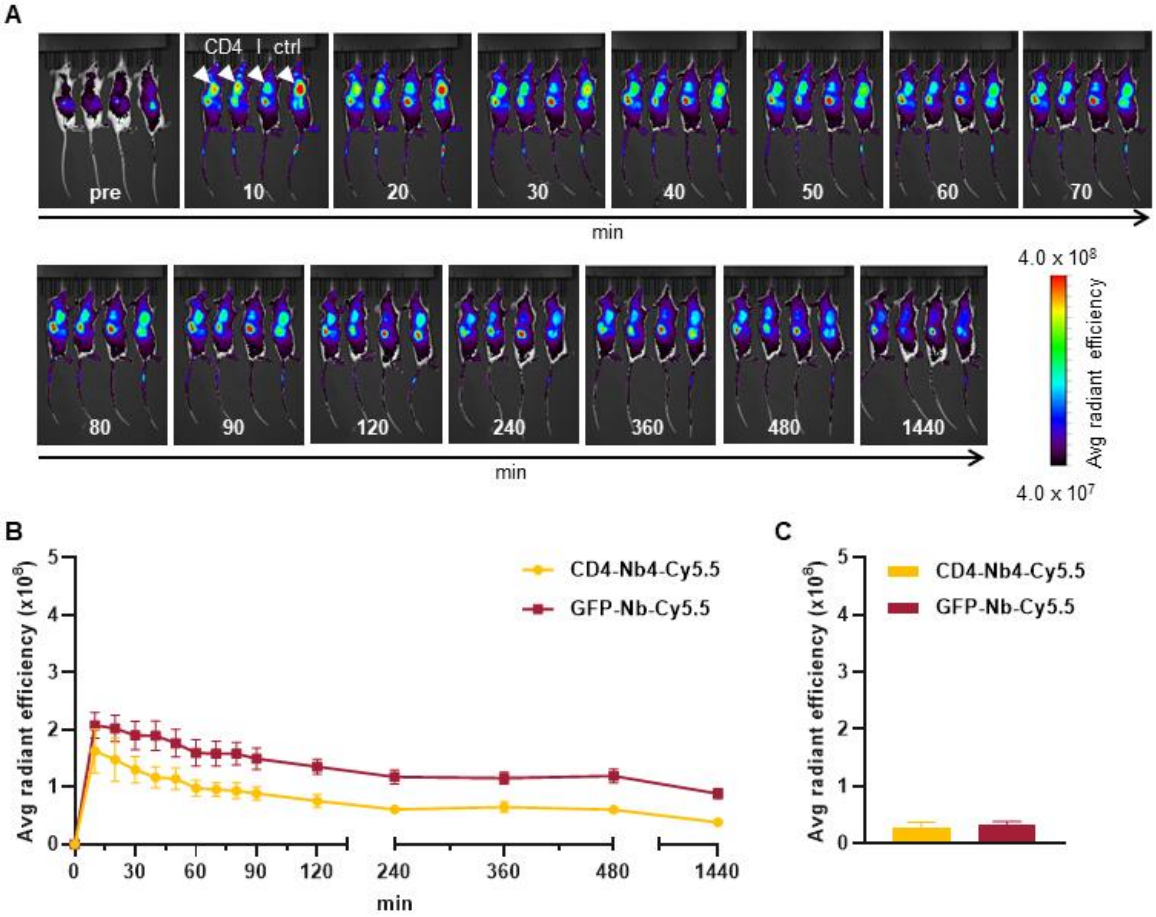

Supplementary Figure 9 *In vivo* optical imaging (OI) of low-affinity binding CD4-Nb4-Cy5.5. 5 µg of CD4-Nb4-Cy5.5-or GFP-Nb-Cy5.5 were administered *i.v.* to *subcutaneously* human $CD4^+$ HPB-ALL-bearing NSG mice and tumor bio distribution was monitored by repetitive OI measurements over the course of 24 h. (**A**) Representative images of each measurement time point of 4 mice injected either with CD4-Nb4-Cy5.5 (left, CD4) or GFP-Nb-Cy5.5 (right, ctrl). White arrows indicate the tumor localization at the right upper flank. (**B**) Quantification of the fluorescence signal from the tumors (n = 4 per group, arithmetic mean of the average radiant efficiency ± SEM). (**C**) After the last imaging time point, tumors were explanted for *ex vivo* OI, demonstrating similar accumulation of CD4-Nb4-Cy5.5 and GFP-Nb-Cy5.5 (n = 2 per group, arithmetic mean ± SEM)

bioRxiv preprint doi: https://doi.org/10.1101/2021.07.02.450848; this version posted July 4, 2021. The copyright holder for this preprint (which was not certified by peer review) is the author/funder, who has granted bioRxiv a license to display the preprint in perpetuity. It is made available under aCC-BY-NC-ND 4.0 International license.

Supplementary Figure 10

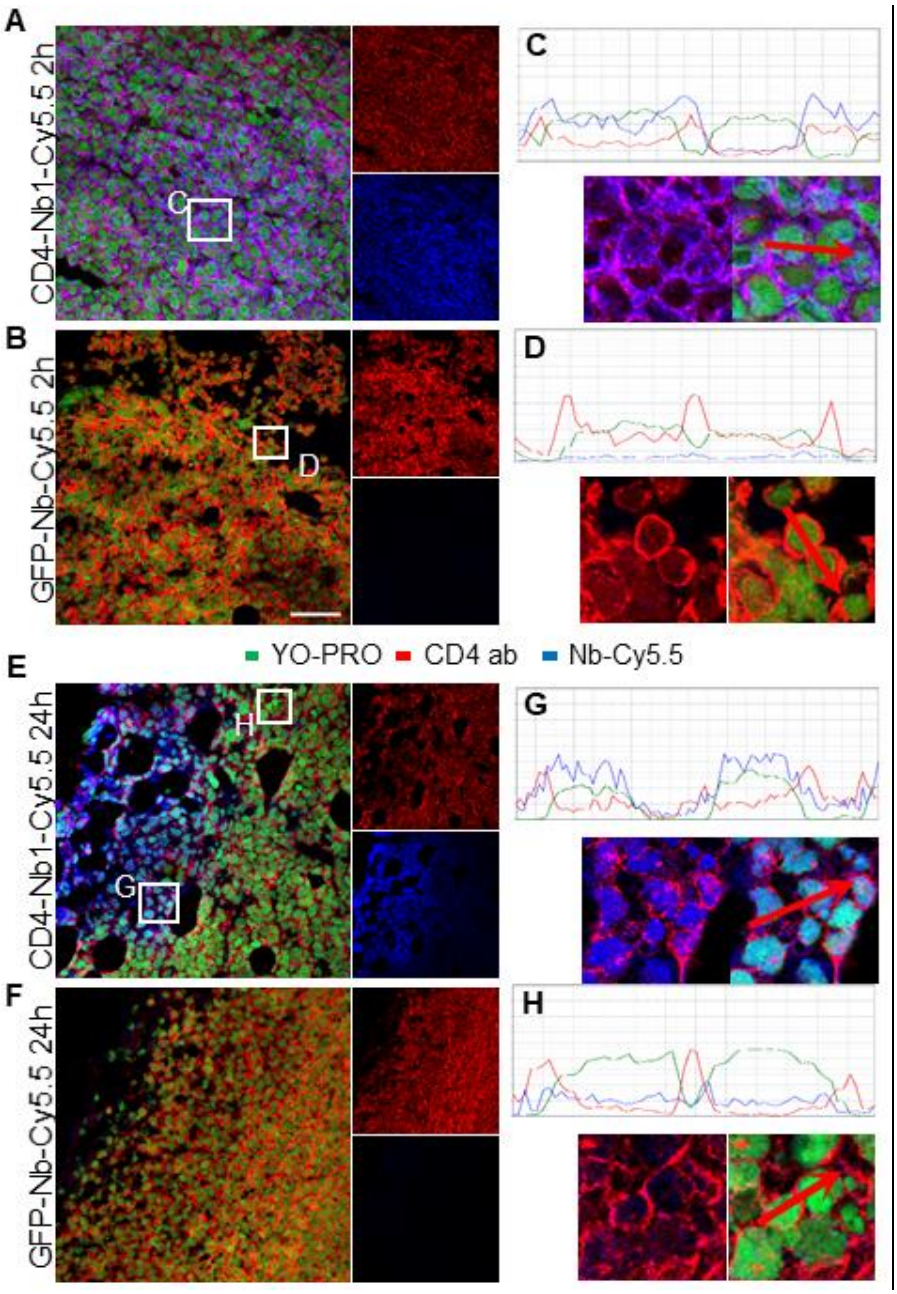

Supplementary Figure 10 Immunofluorescence staining of *ex vivo* HPB-ALL tumors. Cryosections from *ex vivo* HPB-ALL tumors were imaged for bound Nb (blue) from the systemic injection in xenografted mice and co-stained with CD4-specific antibody (red) and nuclear YO-PRO staining (green). Image overlay of CD4-Nb1 (**A**) or control GFP-Nb (**B**) with CD4 antibody fluorescence after 2 hours of Nb injection. (**C**, **D**) Line-scan quantification of indicated image sections from A and B. (**E**, **F**) same as A and B after 24 h of systemic Nb injection. (**G**, **H**) Line-scan analysis of indicated image sections from E of strongly stained area (G) or weakly stained area (H).

bioRxiv preprint doi: https://doi.org/10.1101/2021.07.02.450848; this version posted July 4, 2021. The copyright holder for this preprint (which was not certified by peer review) is the author/funder, who has granted bioRxiv a license to display the preprint in perpetuity. It is made available under aCC-BY-NC-ND 4.0 International license.

Supplementary Figure 11

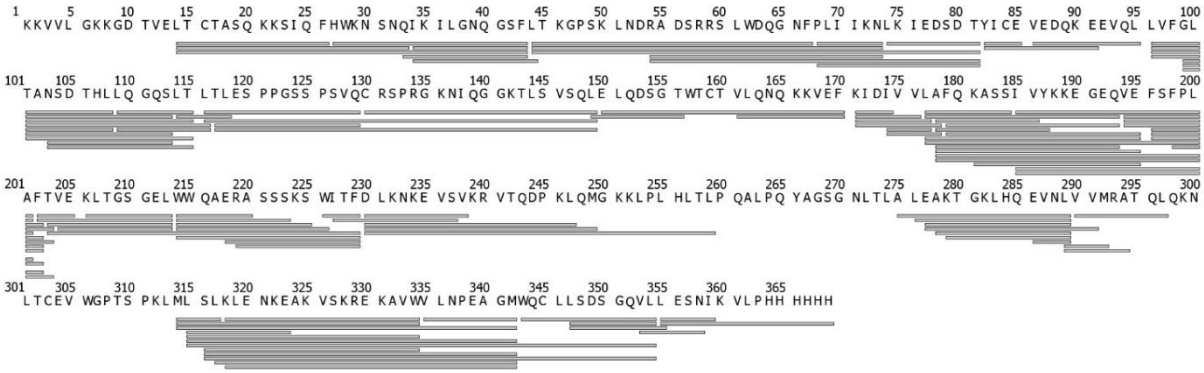

Supplementary Figure 11 Peptide sequence coverage of CD4 for HDX-MS analysis. 116 possible peptides could be identified by MSMS (depicted as bars) leading to a sequence coverage of 88% for the HDX analysis.

bioRxiv preprint doi: https://doi.org/10.1101/2021.07.02.450848; this version posted July 4, 2021. The copyright holder for this preprint (which was not certified by peer review) is the author/funder, who has granted bioRxiv a license to display the preprint in perpetuity. It is made available under aCC-BY-NC-ND 4.0 International license.

Supplementary Methods

Name	Sequence 5´- 3´	purpose
CALL001	GTCCTGGCTGCTCTTCTACAAGG	Nb library generation
CALL002	GGTACGTGCTGTTGAACTGTTCC	Nb library generation
FR1-1	CAT GGC NSA NGT GCA GCT GGT GGA NTC NGG NGG	Nb library generation
FR1-2	CAT GGC NSA NGT GCA GCT GCA GGA NTC NGG NGG	Nb library generation
FR1-3	CAT GGC NSA NGT GCA GCT GGT GGA NAG YGG NGG	Nb library generation
FR1-4	CAT GGC NSA NGT GCA GCT GCA GGA NAG YGG NGG	Nb library generation
FR1-ext1	GTAGGCCCAGCCGGCCATGGCNSANGTGCAGCTGGTGG	Nb library generation
FR1-ext2	GTAGGCCCAGCCGGCCATGGCNSANGTGCAGCTGCAGGA	Nb library generation
FR4-1	GAT GCG GCC GCN GAN GAN ACG GTG ACC NGN RYN CC	Nb library generation
FR4-2	GAT GCG GCC GCN GAN GAN ACG GTG ACC NGN GAN CC	Nb library generation
FR4-3	GAT GCG GCC GCN GAN GAN ACG GTG ACC NGR CTN CC	Nb library generation
FR4-4	GAT GCG GCC GCR CTN GAN ACG GTG ACC NGN RYN CC	Nb library generation
FR4-5	GAT GCG GCC GCR CTN GAN ACG GTG ACC NGN GAN CC	Nb library generation
FR4-6	GAT GCG GCC GCR CTN GAN ACG GTG ACC NGR CTN CC	Nb library generation
NGS fwd	ACACTCTTTCCCTACACGACGCTCTTCCGATCTGGATTGTTATTACTCGCGGCC	library PCR for NGS
NGS rev	GACTGGAGTTCAGACGTGTGCTCTTCCGATCTGATCAGCTTCTGTTCTGCGGC	library PCR for NGS
hCD4 fwd	GGAGGATCCACAATGAACCGGGGAGTCCCTT	hCD4 expression
hCD4 rev	GGTCTCGAGTCAAATGGGGCTACATGTCTTCTGA	hCD4 expression
bsd fwd	ATACCCGGGGCCACCATGGCCAAGCCTTTGTCTC	hCD4 expression
bsd rev	TATGCGCGCTTAGCCCTCCCACACATAACCAG	hCD4 expression
ΔD1 fwd	GCAGTCTCTCACTGGAGCAGCGCGTTCGGATTGACTGCCAACTCTGACACC	CD4_ΔD1 expression
ΔD1 rev	GCGCACGCGATCAGGCATTCCCTGAGTGGCTGCTGGGAGG	CD4_ΔD1 expression
ΔD1ΔD2 fwd	GCAGTCTCTCACTGGAGCAGCGCTTTCCAGAAGGCCTCCAGCATAG	CD4_ΔD1ΔD2 expr.
ΔD1ΔD2 rev	GCGCACGCGATCAGGCATTCCCTGAGTGGCTGCTGGGAGG	CD4_ΔD1ΔD2 expr.
ΔD3ΔD4 fwd	CCCACATGGTCCACCCCG	CD4_ΔD3ΔD4 expr.
ΔD3ΔD4 rev	AGCTAGCACCACGATGTCTATTTTG	CD4_ΔD3ΔD4 expr.
CD4-D1-4 f	ATACGTCTCAACTCTAAGAAAGTGGTGCTGGGCAAAAAAGG	CD4-D1-4 production
CD4-D1-4 r	TATGAATTCAGTGGTGATGGTGGTGGTGGGGCAGAACCTTGATGTTGGATTCC	CD4-D1-4 production

Table S1: primers used in this study

bioRxiv preprint doi: https://doi.org/10.1101/2021.07.02.450848; this version posted July 4, 2021. The copyright holder for this preprint (which was not certified by peer review) is the author/funder, who has granted bioRxiv a license to display the preprint in perpetuity. It is made available under aCC-BY-NC-ND 4.0 International license.

Cytokine	**indicative for**
Interleukin 1 β (IL-1β)	proinflammatory
Interleukin 1 receptor antagonist (IL-1RA)	antiinflammatory
Interleukin 4 (IL-4)	antiinflammatory
Interleukin 6 (IL-6)	pro-/antiinflammatory
Interleukin 8 (IL-8)	proinflammatory
Interleukin 10 (IL-10)	antiinflammatory
Interleukin 12 p70 (IL-12p70)	proinflammatory
Interleukin 13 (IL-13)	antiinflammatory
Granulocyte-macrophage colony-stimulating factor (GM-CSF)	pro-/antiinflammatory
Interferon γ (IFNγ)	proinflammatory
Monocyte chemoattractant protein 1 (MCP-1)	proinflammatory
Macrophage inflammatory protein 1 β (MIP-1 β)	proinflammatory
Tumor necrosis factor α (TNF-α)	proinflammatory
Vascular endothelial growth factor (VEGF)	wound healing factor

Table S2: cytokines analyzed in this study

bioRxiv preprint doi: https://doi.org/10.1101/2021.07.02.450848; this version posted July 4, 2021. The copyright holder for this preprint (which was not certified by peer review) is the author/funder, who has granted bioRxiv a license to display the preprint in perpetuity. It is made available under aCC-BY-NC-ND 4.0 International license.

Table HDX summary	
State	CD4 & CD4 bound by Nb1; Nb2; Nb3
HDX reaction details	1 x PBS pH 7.4, 25 °C, 90% D_2O
Time points	5 & 50 min
Av. back exchange (Synthetic peptides)	24 %
Digest conditions	2 min in an water ice-bath, 30 µl pepsin beads
Number of identified Peptides /Sequence coverage	116 / 88 %
Average peptide length / average redundancy	14.6 (Std. Dev. 8.3) / 4.6
Technical replicates (triplicate)	min 2 of 3 peptides per time point, in both states
Determined ΔHX threshold for each time point	0.25 – 0.27 Da
Significant differences in HDX	Students t-distribution on 95% confidence level

Table S3: HDX-MS Summary

bioRxiv preprint doi: https://doi.org/10.1101/2021.07.02.450848; this version posted July 4, 2021. The copyright holder for this preprint (which was not certified by peer review) is the author/funder, who has granted bioRxiv a license to display the preprint in perpetuity. It is made available under aCC-BY-NC-ND 4.0 International license.